Simultaneous Hydrogen and Oxygen Evolution Reactions using Free-Standing Nitrogen-Doped-Carbon-Co/CoOx Nanofiber Electrodes Decorated with Palladium Nanoparticles

Ahmed Barhoum, Heba H El-Maghrabi, Amr A Nada, Syreina Sayegh, Stéphanie Roualdès, Aurélien Renard, Igor Iatsunskyi, Emerson Coy, Mikhael Bechelany

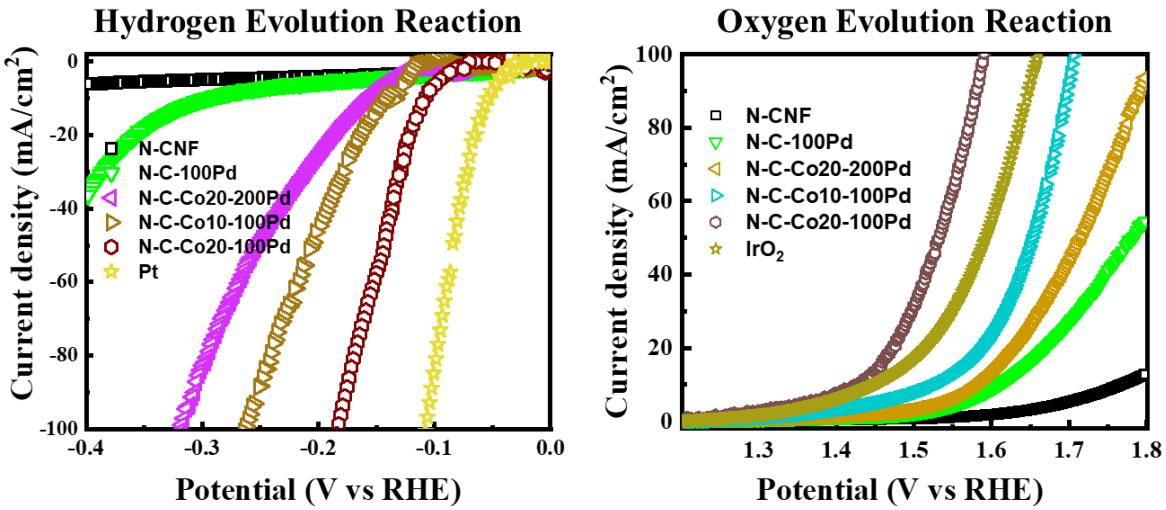

Simultaneous Hydrogen and Oxygen Evolution Reactions using Free-Standing Nitrogen-Doped-Carbon-Co/CoO_x Nanofiber Electrodes Decorated with Palladium Nanoparticles

Ahmed Barhoum,[1,2,3*] Heba H. El-Maghrabi,[2,4] Amr A. Nada,[2,5] Syreina Sayegh,[2] Stéphanie Roualdes[2], Aurélien Renard,[6] Igor Iatsunskyi,[7] Emerson Coy,[7] Mikhael Bechelany[2*]

[1] Chemistry Department, Faculty of Science, Helwan University, Cairo 11795, Helwan, Egypt

[2] Institut Européen des Membranes (IEM), UMR 5635, Univ Montpellier, ENSCM, CNRS, Place Eugène Bataillon, 34095 Montpellier, France

[3] School of Chemical Science, Dublin City University, Dublin 9, Ireland

[4] Dept. of Refining, Egyptian Petroleum Research Institute, Cairo, Nasr city P.B. 11727, Egypt.

[5] Dept. of Analysis and Evaluation, Egyptian Petroleum Research Institute, Cairo, Nasr city P.B. 11727, Egypt.

[6]LCPME - UMR 7564 - CNRS - Université de Lorraine, 405, rue de Vandoeuvre, 54600 VILLERS-LES-NANCY, France

[7]NanoBioMedical Centre, Adam Mickiewicz University, 3 Wszechnicy Piastowskiej str., 61-614, Poznan, Poland

Corresponding authors: ahmed.barhoum@science.helwan.edu.eg, ahmed.barhoum@dcu.ie

mikhael.bechelany@umontpellier.fr

Abstract

Designing efficient electrode materials for electrochemical water splitting is the most critical challenge for next-generation hydrogen fuel production. This study describes the development of free-standing nitrogen-doped carbon nanofiber (N-CNF) electrodes that incorporated cobalt/cobalt oxide (Co/ CoO_x) nanoparticles (NPs) and were decorated with palladium NPs (Pd NPs). These free-standing electrodes displayed high electrocatalytic activity during electrochemical water splitting, and were fabricated in three steps: (i) solution electrospinning of polyacrylonitrile (PAN)/cobalt acetate nanofiber mats; (ii) PAN/cobalt acetate nanofiber mat peroxidation and stabilization in air atmosphere followed by pyrolysis (carbonation) in nitrogen atmosphere; and (iii) decoration of the electrode surface with 5 and 10 nm Pd NPs by controlled atomic layer deposition (ALD) (100 and 200 cycles, respectively). The N-CNF-Co/CoO_x-Pd electrode performance was tested in simultaneous hydrogen/oxygen evolution reactions (HER/OER) with an alkaline electrolyte solution (1 M KOH). The electrodes were as electroactive as Pt and IrO_2 (reference electrodes) for overall electrochemical water splitting. The most efficient electrode displayed very interesting overpotential (100 mV and 160 mV @ j = 10 mA cm^{-2} for HER and OER, respectively), Tafel slope (33 and 113 mV dec^{-1}), and exchange current density (1.15 and 22.4 mA cm^{-2}) values. Interestingly, electrodes with the smallest Pd NP size (5 nm/100 ALD cycles) showed higher electrocatalytic activity for HER and OER than electrodes coated with bigger particles (10 nm/200 ALD cycles) and the reference Pt electrode. The effect of Co/CoO_x NP encapsulation in the graphitic layers of N-CNFs and coating with Pd NPs on the electrode electrocatalytic activity are discussed in detail.

Keywords: Electrochemical Water Splitting, Heterostructure Electrocatalyst, Electrospinning, Atomic Layer Deposition, Nitrogen-doped Carbon Nanofibers, Cobalt-Cobalt Oxide Heterojunction, Graphitic Layer Structures

1. Introduction

Hydrogen is particularly interesting as a green fuel to meet the global energy demand. It can be produced from water splitting without emission of any pollution. Moreover, when it recombines with oxygen in fuel cells, it produces electrical energy and water only as a by-product.[1–3] These characteristics make hydrogen an attractive fuel for electricity generation applications (e.g. cars, trains, ships, aircraft, portable power, and houses).[4] Water splitting (HOH) to generate H_2 and O_2 can be performed via an electrochemical reaction using two electrodes and an aqueous electrolyte solution (acidic or alkaline).[5,6] For practical uses, electrochemical water splitting powered by photovoltage (PV) cells is also under development. Electrocatalysts accelerate electron transfer between electrode and reactants and also increase the speed of the intermediate chemical transformation during each half-reaction (i.e. hydrogen evolution reaction and oxygen evolution reaction, HER, and OER).[7,8] Conversely, the electrocatalyst overpotential limits the efficiency of electrochemical water splitting. These overpotentials can be significantly reduced using electrocatalysts that harbor active sites for HER/OER. To date, Pt and Pt/C (for HER) and IrO_2 and RuO_2 (for OER) are considered the most powerful electrodes with the lowest overpotential.[9] However, their industrial applications are limited because they are very expensive and rare.[10–12] Indeed, electrode activity, cost, durability, and stability are of major importance. Therefore, it is crucial to develop efficient and cheap electrocatalysts for HER/OER to meet the increasing industrial demands.[13]

Carbon nanofibers (CNFs) incorporating metal and metal oxide nanoparticles (NPs) are interesting materials for electrochemical water splitting because of their high dimensional stability, large specific surface, good electrical conductivity, and electrocatalytic activity, and also ability to minimize electrode surface fouling.[14–16] CNF-based electrodes are among the most interesting electrode materials for water treatment,[17–19] electrochemical biosensing,[20–22,23,24,25] batteries,[26] supercapacitors,[26,27] and drug delivery.[28,29] The interpenetrating CNF network offers many active

sites, good electrical conductivity, mechanical stability, and electrolyte diffusion.[30] It has been shown that many transition metals (e.g. Cu,[14] Mo,[31] W,[32] Co,[33] Ni,[34], and Fe[35]) are efficient electrocatalysts for HER and OER.[14,15,16] Transition metal/metal oxide NPs incorporated in CNFs also show superior electrocatalytic activity, stability, and selectivity in HER/OER.[36,37] Other cheap and effective electrode materials for HER/OER include transition metal carbides,[38] perovskites (ABO_3 in which A and/or B are transition metals), and oxide spinel (AB_2O_4 in which A and/or B are transition metals). However, in HER/OER tests, they show poor performances due to their low electrical conductivity and corrosion.[12]

Recently, atomic layer deposition (ALD) has been used as a cost-effective technique to deposit small amounts of expensive electrocatalyst NPs on the CNF electrode.[39] The electrocatalytic activity of ALD-deposited catalyst NPs is strongly influenced by their amount, size, geometry, and their distribution within the electrode surface/porous structure.[40] ALD allows controlled deposition of noble metal NPs with controlled morphologies and compositions (monometallic,[41] bimetallic,[42] and core–shell[43]), depending on the application.[44] Comparing with Pt and Au NPs, ALD of the Pd NP on the CNF electrode surface can enhance its electrochemical activity, improve chemical stability, and reduce the overpotential of HER and the overall cost.[45,46] As controlled ALD allows reducing the Pd NP size to atomic clusters or even single atoms, it could lead to a major reduction of the Pd NP mass on the electrode surface and enhance the electrode electrochemical activity towards HER/OER reaction.[27,47,48] However, the impact of the deposited layer thickness, heterojunctions, and nanointerfaces on the CNF electrocatalytic activity has not been thoroughly investigated yet.[49,50,51] Aside from ALD of electrocatalyst catalyst NPs

Recent progress in electrospinning technique led to the development of low-cost electrospun CNFs electrodes incorporating transition metals NPs with improved electrocatalytic activity towards HER/OER reactions close to Pt, Pt/C, IrO_2, and RuO_2 based electrodes.[52] However, there is no studies have been published on the potential applications of free-standing CNF electrodes that

incorporate Co/CoO_x NPs as electrocatalyst and are decorated with Pd NPs (by ALD) for simultaneous HER and OER. This study aims to study simultaneous hydrogen and oxygen evolution reactions using free-Standing nitrogen-doped-carbon-Co/CoOx nanofiber electrodes decorated with Pd NPs. The free-standing nitrogen-doped CNF (N-CNFs) and N-CNF-cobalt/cobalt oxide (Co/CoO_x)-Pd electrodes were produced in a multistep process in which a polyacrylonitrile (PAN) and cobalt acetate solution were electrospun to fabricate free-standing and binder-free N-CNF mats with Co/CoO_x NPs that were thermally stabilized under air and carbonated under nitrogen. Finally, the electrode surface was decorated with Pd NPs by ALD. The N-CNF-Co/CoO_x-Pd heterostructure provided an excellent electrocatalytic activity for HER/OER in an aqueous alkaline electrolyte (1 M KOH) with high chemical stability. The formation of graphitic layers in the N-CNF matrix facilitated Co/CoO_x dispersion into the N-CNF bulk and on the electrode surface. The N-CNF architecture also favored the electrolyte accessibility to active Co/CoO_x and Pd NP sites and increased electron transfer between electrode and electrolyte. Furthermore, Co/CoO_x embedding in the graphitic layers and Pd NP deposition by ALD protected the Co/CoO_x NPs from oxidation and corrosion during HER/OER and significantly increased the electrode durability.[26] By controlling the electrode composition and electrolysis conditions, the fabricated N-CNF-Co/CoO_x-Pd electrodes displayed very good electrochemical activity (low overpotential values and Tafel slope during HER/OER) and stability relative to the reference Pt electrode.

2. Experimental

2.1. Materials

Polyacrylonitrile (PAN, Mwt ~150000, CAS 25014-41-9, Sigma-Aldrich), cobalt (II) acetate tetrahydrate ($Co(OCOCH_3)_2 \cdot 4H_2O$, 99%, CAS No. 6147-53-1, Sigma-Aldrich), N,N-dimethylformamide (DMF, 98%, CAS No. 68-12-2, Sigma-Aldrich) and ethanol (C_2H_5OH, 99%, CAS No. 64-17-5, Sigma-Aldrich) were used for fabricating free-standing N-CNF-Co/CoO_x

electrodes by electrospinning. Palladium (II) hexafluoroacetylacetonate ($Pd(C_5HF_6O_2)_2$, CAS 64916-48-9, 99%, Sigma-Aldrich) was used as Pd precursor and formaldehyde (HCHO, CAS No. 50-00-0, 37%, Sigma-Aldrich) as co-reactant for ALD deposition of Pd NPs on N-CNF-Co/CoO_x electrodes. Potassium hydroxide (KOH, CAS 1310-58-3, Sigma-Aldrich) and sulfuric acid (H_2SO_4, CAS No. 7664-93-9, 97%, Sigma-Aldrich) were used as an electrolyte solution for the HER and OER tests.

2.2. Fabrication of Free-Standing Nanofiber Electrodes

Three N-CNF mats incorporating Co/CoO_x NPs were produced according to the following three-step procedure: i) electrospinning; ii) thermal oxidation, and iii) thermal pyrolysis.[53] Briefly, the PAN/cobalt acetate/DMF solution was prepared by dissolving an appropriate amount of cobalt (II) acetate tetrahydrate in 20 mL DMF, and then by adding PAN powder to the mixture that was continuously stirred for 15h to obtain a homogenous solution. Electrospinning was performed with solutions that contained 0%, 10%, or 20% cobalt acetate and loaded in 20 mL plastic syringes and the following parameters: tip-to-collector distance = 15 cm, operating voltage = 25 kV, flow rate = 1 ml/min, and drum rotating speed = 400 rpm. Then, the nanofiber mats underwent thermal peroxidation for 2h (250 °C, air atmosphere) and pyrolysis for 1h (1000 °C, nitrogen atmosphere, constant heating and cooling rate of 1 °C.min^{-1}).

2.2. Decoration with Pd NPs (Co-catalyst) by ALD

The N-CNF-Co/CoO_x surface (electrode) was decorated with Pd NPs (co-catalyst) by performing 100 or 200 ALD cycles[48] using a home-made ALD reactor and $Pd(hfac)_2$ (i.e. the Pd precursor, heated to approximately 70 °C to achieve the appropriate vapor pressure), formalin (i.e. the reacting species, kept at 25 °C) and argon (Ar, i.e. the purging gas). The ALD lines were at 100 °C and the deposition chamber at 220 °C. A typical ALD cycle included a 5 seconds pulse of $Pd(hfac)_2$ with an exposure time of 15 seconds followed by Ar purge for 10s, and finally, 1 seconds pulse of formalin for 15 seconds and Ar purge for 60 seconds, as previously described.[54,55]

2.3. Characterization of the Prepared Electrodes

The crystal structure and crystallite size of the fabricated electrodes were analyzed by X-ray diffraction (XRD) with a PANAlytical Xpert-PRO device with Ni-filtered Cu-radiation (wavelength of 0.154 nm) as a radiation source. Their fiber diameter and surface morphology, composition, and crystallinity were measured by scanning electron microscopy (SEM, Hitachi S4800 microscope, Japan Zeiss EVO HD15 microscope) and high-resolution transmission electron microscopy (HR-TEM, JEOL ARM 200F, Japan) with an energy dispersive X-ray (EDX) analyzer. Raman spectra were recorded with a SENTERRA Raman microscope spectrometer (Bruker, Germany) with the double-frequency Nd:YAG and 532 nm lasers. X-ray photoelectron spectroscopy (XPS) was performed using a Kratos Axis Ultra spectroscope (Kratos Analytical, UK) and a monochromatic Al K_{α} source (1486.6 eV). Co elemental concentration in the as-prepared N-CNFs was determined by atomic absorption spectroscopy (ASS, AAnalyst 400, PerkinElmer). The mean pore diameter, volume, and surface area were assessed from the N_2 adsorption-desorption isotherms using the BET method (Brunauer Emmett and Teller, Micromeritics ASAP 2010 equipment).

2.4. Electrochemical Tests

For HER and OER, a CHI 660E workstation was used with: (i) free-standing N-CNF, N-CNF-Co/CoO_x, and N-CNF-Co/CoO_x-Pd electrodes as working electrodes (obtained by cutting the prepared electrodes into circles with diameter =1 cm and thickness = 0.25 mm); (ii) a silver/silver chloride electrode as reference electrode (Potentials were referenced to a reversible hydrogen electrode (RHE) following the equation: $E_{RHE} = E_{Ag/AgCl} + 0.059 \times pH + 0.197$); and (iii) a graphitic electrode as counter electrode. For all tests, 1 M KOH was used as the electrolyte solution. In HER and OER tests, the fabricated electrodes were tested alongside commercial Pt and IrO_2 electrodes (working electrodes), respectively. All spectra were acquired after 10 cycles at a 100 mV s^{-1} scan rate to trigger and stabilize the prepared electrodes. Cycle sweep voltammetry (CSV) and linear sweep voltammetry (LSV) data were collected at a 5 mV s^{-1} scan rate for all tests. Electrochemical

impedance spectrometry (EIS) was performed from 10^{-1} to10^{5} Hz at -0.3 V vs RHE and at 1.6 V vs RHE, for the HER and OER tests, respectively. To assess the electrocatalytic stability during HER, the chronoamperometric response (i-t curves) was recorded in 1 M KOH solution and -0.3 V vs. RHE for 12h. Hydrogen evolution was monitored by gas chromatography (Clarus-400, PerkinElmer, TCD (2m x1mm), He carrier) of gas samples collected with a syringe every 30 min at 100 mV. Faradaic efficiency (FE) was calculated using the following equation: FE (%) = [2F * mol H_2 (GC) * 100] / [Q], where F is the Faraday constant, Q is the gas volume % based on the charge passed, and GC is the gas volume %.[56]

3. Results and Discussion

Through HER and OER, water electrolysis leads to the production of hydrogen fuel and oxygen gas, respectively. Among the different types of electrode materials, N-CNFs represent an excellent scaffold to support electrocatalytic metal NPs. In this study, free-standing N-CNF electrodes incorporating Co/CoO_x NPs and coated with Pd NPs were developed and tested. Due to its high mechanical strength, excellent electrical conductivity, and elevated carbon yield (>65% wt/wt), PAN is the most promising polymer for N-CNF electrode production. Nitrogen doping of CNFs and incorporation of Co/CoO_x NPs were performed by electrospinning a cobalt acetate-PAN solution, followed by ALD of PD NPs (Scheme 1).

During the peroxidation step, PAN or PAN-cobalt acetate nanofibers undergoes different chemical process such as oxidation, cyclization, crosslinking, aromatization and dehydrogenation that make the polymer (PAN or cobalt acetate/PAN) fibers denser and more thermally stable during the subsequent thermal carbonation step. This step prevents the fusion of individual fibers before furthering the carbonization step, by inducing additional oxygen into the PAN structure. In the subsequent step (thermal carbonation), nanofibers (PAN or cobalt acetate/PAN) begin to pyrolysis with a considerable release of volatile by-products. The characteristics of the CNFs are typically

influenced by the thermal treatment parameters, especially the nature of gas, heating rate, the final temperature, and the time of the isothermal treatment.[57] T. Wanjun and C. Donghua[58] studied the mechanism of thermal decomposition of cobalt acetate tetrahydrate in N_2 and H_2 atmosphere. The authors reported that the residual compositions in the above processes were similar regardless of the atmosphere used. The dehydration process was followed by a major step concerning the decomposition of the acetate group, leading to basic acetate as an intermediate, which then produced CoO and Co in N_2 and H_2 atmosphere, respectively. These findings are in agreement with our results that indicate the in-situ formation of the CoOx/Co NPs inside the CNFs during the thermal carbonation under nitrogen atmosphere.[58]

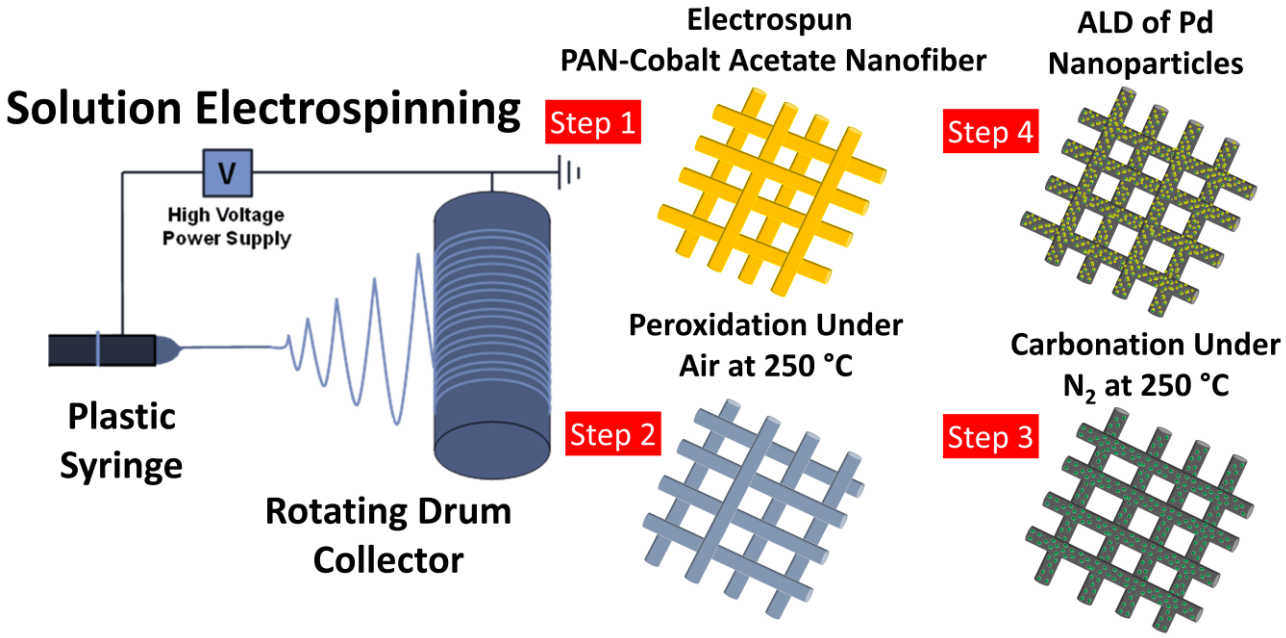

Scheme 1. Four main steps of the production of Free-Standing Nitrogen-Doped-Carbon-Co/CoOx Nanofiber Electrodes Decorated with Palladium Nanoparticles

By encapsulating Co/CoO_x NPs into graphitic layers of N-CNFs, Co/CoO_x NP agglomeration and migration can be efficiently reduced. This also limits the corrosion and oxidation of the fabricated electrodes caused by the electrolyte. Therefore, N-CNFs are often chosen as the main component to enhance electrochemical stability, active site density, and electron/electrolyte transfer on the electrode surface. Moreover, the nitrogen atoms (oxidized N, pyrrolic, pyridinic, graphitic)[59] used for doping can interact with three C atoms at different locations on the graphene layer, strongly improving the electrode conductivity and electrochemical properties. As water electrolysis is generally performed in the presence of alkaline electrolyte solutions, rather than acidic electrolyte solutions, the developed electrode materials should show satisfactory performance in basic media. In the basic electrolyte solution (1 M KOH) used in this study, the Co atoms on the Co/CoO_x NP surface can be transformed into $Co(OH)_2$, which is an active-active phase for OER. Conversely, in the presence of an acidic electrolyte solution (0.5 M H_2SO_4), Co/CoO_x NPs tend to be corroded and passivated during HER and OER.

3.1. Analysis of the Composite Nanofiber Electrode Composition and Morphology

Morphology and elemental composition of the prepared N-CNF and N-CNF-Co/CoOx electrodes were investigated by field-emission SEM and HR-TEM. SEM analysis (Figure 1) showed that the cobalt acetate to PAN weight ratio significantly influenced the size and morphology of the N-CNF, in particular, the number of incorporated Co/CoO_x NPs and their sizes and size distribution. Indeed, the electrodes formed a 3D porous structure with randomly oriented CNF with diameters of 300±44 nm for N-CNF (Figure 1a), 220±33 nm for N-C-Co10 (Figure 1b), and ~200±29 nm for N-C-Co20 (Figure 1c). Diameter of the nanofibers depends mainly on solution properties. The addition

of cobalt acetate changes the solution properties i.e., it increases the solution's electrical conductivity. The increase in solution electrical conductivity improve the polymer solution spinnability and as a result affects the jet formation and decreases fiber diameter.[60] As the cobalt acetate to PAN weight ratio increased from N-C-Co10 to N-C-Co20, larger numbers of rhombohedral Co/CoO_x NPs were formed inside the N-CNFs and they covered also the N-CNFs surface (Figure 1b,c). The particle size of Co/CoO_x NP located at the N-CNF surface slightly increased from 20-50 nm to 30-80 nm with the increase of the cobalt acetate percentage from N-C-Co10 to N-C-Co20, respectively (Figure 1b,c). The elemental composition analysis (representative SEM-EDX results in Figure 1d) confirmed that: (i) the elements C, Co, N, and O were homogeneously distributed, (ii) the thermal pyrolysis of thermally treated PAN/cobalt acetate nanofibers under nitrogen atmosphere allows for nitrogen-doping of CNFs which might contribute to the electrode's excellent electrochemical activity. The ASS analysis indicated that Co total content was approximately 14wt% for N-C-Co10 and 25wt% for N-C-Co20 (Table S1, Supplementary Materials).

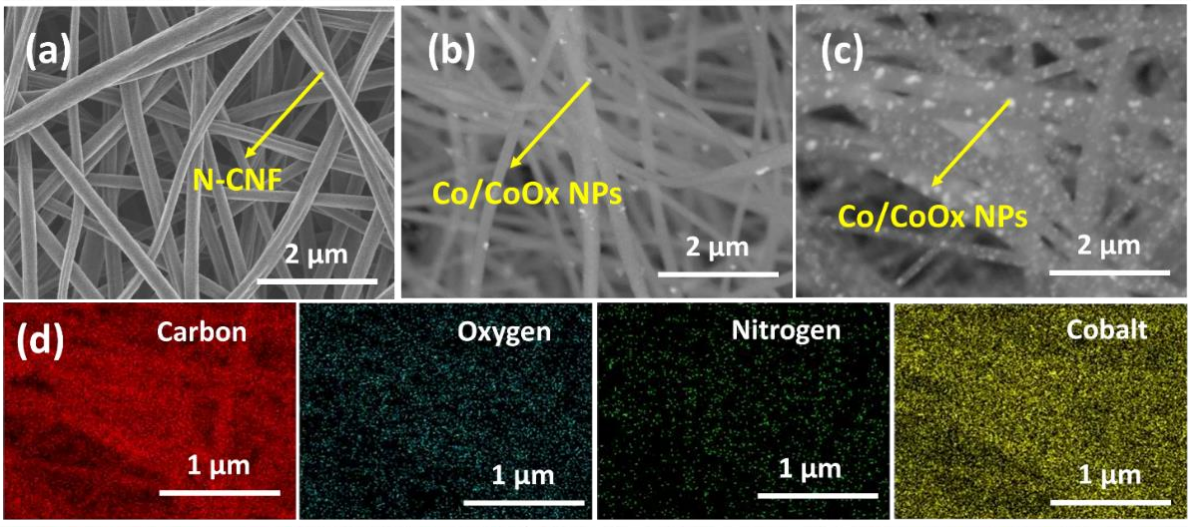

Figure 1. Field-emission SEM photographs of the fabricated free-standing electrodes: (a) N-CNF; (b) N-C-Co10; (b) N-C-Co20; and (d) SEM EDX-based elemental mapping of N-C-Co20.

HR-TEM analysis (Figure 2) showed that Co and Pd NPs were firmly attached to the N-CNF surface (Fig. 2d). Unlike SEM, the TEM has a much higher resolution but allows less amount of

sample to be analyzed at a time. TEM images in Figure 2a-b show that the N-C-Co20-Pd100 surface was covered by 40±10 nm Co/CoO_x NPs and 7±2 Pd NPs. Higher magnification TEM images (Figure 2e) indicated that Co/CoOx NPs were coated by a graphitic layer and that Pd NPs were deposited conformably on the graphitic layers. TEM-EDX (Figure 2d) with elemental mapping confirmed C, Co, and Pd homogeneous distribution at the N-C-Co20-Pd100 surface. Moreover, the lattice spacing of 0.35 nm (inset in Figure 2e) corresponded to the 002 crystal planes of the graphitic layers, in agreement with the XRD results. The TEM and SEM results indicated that the electrodes were made of interpenetrated crystalline graphitic layers coated by Co NPs grown *in situ* on the entire framework. Furthermore, the N-CNF architecture inhibited the restacking of graphitic nanosheets. The electrocatalytic activity should progressively increase with Co/CoO_x NP and Pd NP higher dispersion and smaller size and with the presence of graphene layer structures. Similar studies reported that higher catalytic activity is obtained with Pd NPs of a specific size (e.g. 10 nm, Figure 2c,d).[61] Interestingly, in our work, the Pd-graphene-Co/CoO_x nanostructure was observed by HR-TEM (Figure 2d) and confirmed by XPS and Raman spectroscopy (Figure 3b), but was not reported in previous similar studies.[62,63,64]

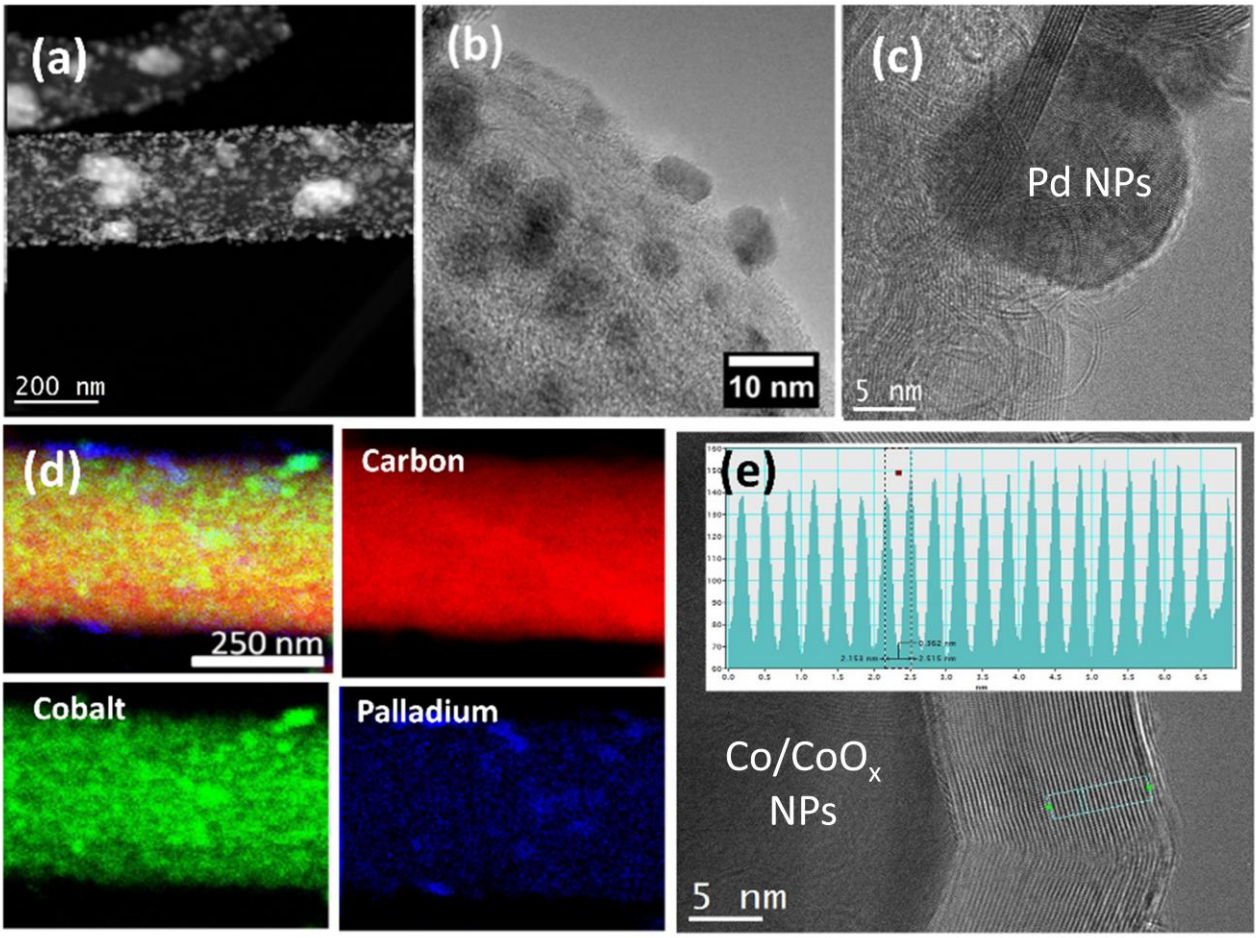

Figure 2. TEM analysis of a free-standing N-C-Co20-Pd100 electrode: (a) Low magnification TEM photograph; (b) high magnification of the nanofiber surface; (c) TEM image of single ALD Pd NPs on the CNF surface; (d) TEM-EDX-based elemental mapping; and (e) High magnification TEM images of Co/CoOx NPs coated with graphitic layers, inset the lattice spacing of the graphitic layers.

XRD analysis was applied for the prepared electrodes (N-CNF, N-C-Co10, and N-C-Co20) to study the effect of cobalt acetate incorporation into the N-CNF crystallinity and crystal structure (Figure 3a,b). XRD analysis showed that the peak at $2\theta = 25°$ was associated with the hexagonal graphite (002) lattice planes (JCPDS card no. 41-1487), with an inner-layer spacing d = 0.336 nm. This suggests that the pristine N-CNF sample has a low degree of graphitization.[65] Conversely, the higher and stronger intensity of the (002) peak intensity in the N-C-Co20 and N-C-Co10 electrodes suggests a higher degree of crystallinity of the carbon matrix and Co/CoOx NPs in these two

samples. Moreover, the higher intensity for the graphitic peak at $2\theta = 25°$ indicated that higher percentage of Co/CoOx NPs accelerate the formation of graphitic carbon. The N-C-Co10 and N-C-Co20 electrodes showed also two sharp peaks at around 44.3° and 54° that were ascribed to the (111) and (200) planes of the fcc crystal structures of metallic Co (JCPDS 15-0806), respectively. The average crystallite sizes of Co/CoO_x NPs, calculated with the Scherrer equation,[66,67,68] were 32.0±0.4 (N-C-Co10) and 35.1±0.3 (N-C-Co20) (Table S1, Supplementary Materials). When we compare the average crystallite size of N-C-Co10 to the average particle size, the average crystallite sizes of these samples are similar or slightly smaller than the average particle size estimated by SEM and TEM while the difference is bigger for N-C-Co20. This indicates that N-C-Co20 contain higher percentage of polycrystalline Co/CoOx NPs, while crystals formed in N-C-Co10 is mainly single crystals; these findings where discussed elsewhere.[69] The production of reducing by-products during thermal carbonization under N_2 atmosphere could explain the presence of metallic Co nanocrystals instead of CoO_x nanocrystals.[70] Therefore, the pre-oxidation step of PNA-cobalt acetate followed by calcination under nitrogen atmosphere is main reason for the formation of CoO_x together with Co. Oxygen content (about 2% according to the SEM-EDX and TEM-EDX analyses with elemental mapping) could be due to minimal N-CNF oxidation or to the generation of amorphous CoO_x impurities during thermal peroxidation after electrospinning. XRD diffraction could not detect other phases (i.e. cobalt oxides, and cobalt carbides) for N-C-Co10 and N-C-Co20 possibly due to their small crystallite size, low content, and/or amorphous nature.[70] However, the two collapsed diffraction peaks observed at 2θ of 44° (Figure 3b) could be explained by the presence of CoO_x, at very low concentration, in the catalyst, as confirmed by XPS and Raman spectrometry. Slight shift in the peak positions could attributed to macrostrain present in the unit cell of the obtained crystals with increasing the cobalt acetate concertation from for N-C-Co10 to N-C-Co20. Previous studies showed that metallic Co^0 and CoO_x can synergistically increase the catalytic performance.[71]

Raman analysis was applied for the prepared electrodes (N-CNF, N-C-Co10, and N-C-Co20) to study the effect of cobalt acetate incorporation into the N-CNF graphitic architecture (Figure 3c). Generally, N-CNF show two main peaks: the broad D band (1300 cm^{-1}; amorphous carbon) and the G band (1600 cm^{-1}; ordered graphitic structure).[72] The relative intensities (R) of these two bands (I_D/I_G) are positively influenced by the number of amorphous carbon (disordered sp^2) and graphitic layers (ordered sp^2 bonding carbon atoms).[65] The D (~1320 cm^{-1}) and G (~1590 cm^{-1}) bands were detected in all analyzed electrode samples (Figure 3c). The I_D/I_G value was 1.13 for pristine N-CNF, but it gradually decreased with the cobalt acetate content: 0.92 for N-C-Co10 and 1.01 for N-C-Co20.[73] With higher Co/CoO_x NP content, the carbonaceous structures should more easily form graphitic structures. Raman spectrometry was used also to investigate the CoO_x structures. The N-C-Co10 and N-C-Co20 spectra showed four typical Co_3O_4 peaks between 474 and 677 cm^{-1} (Figure 3c) that matched the reported CoO_x spectrum.[74] The five Raman peaks for Co_3O_4 at 192, 474, 513, and 667 cm^{-1} are associated with T_2g, Eg, and A_1g symmetries. The presence of Co_3O_4 could be explained by Co NP surface oxidation by oxygen during peroxidation in air atmosphere after electrospinning.[75]

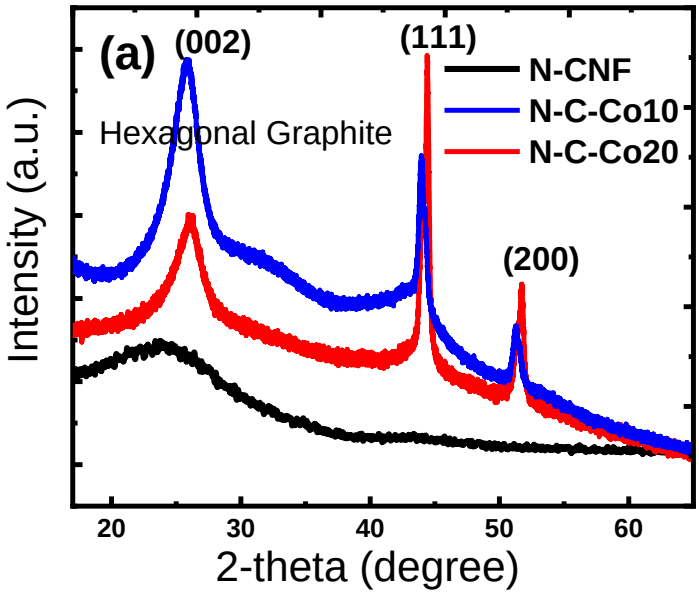
(a)
(002)
(111)
(200)
N-CNF
N-C-Co10
N-C-Co20
Hexagonal Graphite
Intensity (a.u.)
20
30
40
50
60
2-theta (degree)

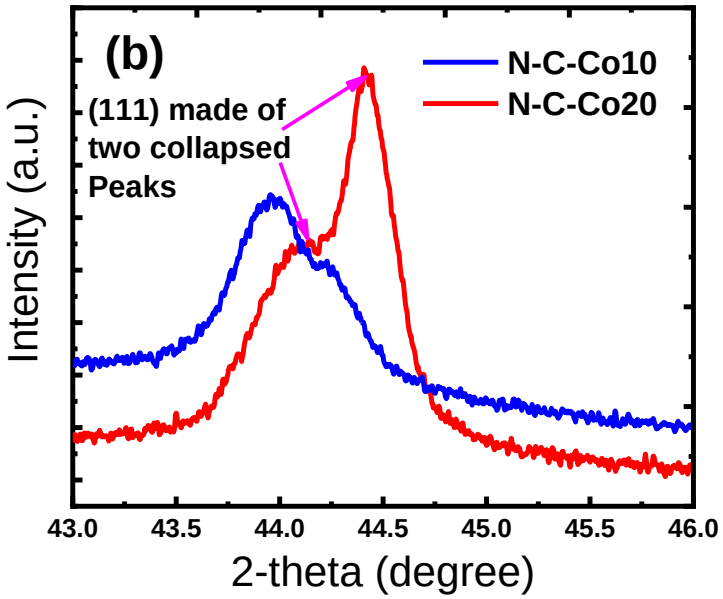
(b)
(111) made of
two collapsed
Peaks
N-C-Co10
N-C-Co20
Intensity (a.u.)
43.0
43.5
44.0
44.5
45.0
45.5
46.0
2-theta (degree)

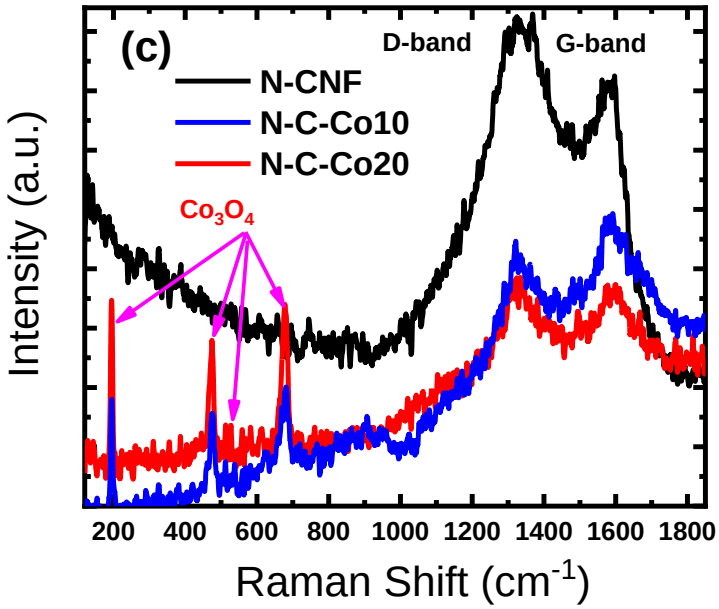

Figure 3. XRD analysis and Raman spectrometry of the indicated free-standing electrodes: (a) XRD patterns, (b) XRD pattern of the (111) plan of Co, and (c) Raman spectra.

XPS can be used to analyze the surface chemistry of the free-standing electrodes before and after ALD on Pd NPs on the electrode surface (Figure 4a). XPS survey spectra (Figure 4a) indicated that N-C-Co20 and N-C-Co20-Pd100 exhibited peaks related to C(1s), O(1s), N(1s), Co(2p), Pd(3d) core levels. When quantified these five peaks, the N-C-Co20 are consisted of 95.1 % C, 2.7% O, 1.4% N, 0.8 % Co, and 0.0% for Pd while the N-C-Co20-Pd100 exhibit 87.7 % C, 2.0% O, 1.0% N, 0.9 % Co, and 8.4% (Table S2, Supplementary Materials). The C1s peak (Figure 4b) comprised four different peaks that might be attributed to sp^2 carbon (C=C) and three low-intensity components (C-C/C-H, 284.9 eV), (C-O, 285.8 eV), (C=O, 287.0 eV). [76] The O1s peak (Figure 4c) could not be decomposed due to charge effects and/or partial overlapping of the O 1s and Pd $3p_{3/2}$ peaks. The high-resolution XPS spectra of N 1s (Figure 4d) point out the existence of N-doping of different nitrogen species pyridinic, nitrile, and quaternary nitrogen, which has a significant effect on HER/OER reactions. The CoO_x (oxidation state) could not be easily quantified because of the low

signal-to-noise ratio. However, we can confirm that the cobalt oxide and a cobalt metal state co-existed.[74] The maximum intensity of the two peaks, observed at 778eV and 780eV, suggested the contribution of metal Co (0) and Co oxide (III) to the spectra (Figure 4e). [70] The high-resolution XPS spectra of Pd 3d (Figure 4f) further confirm Pd NP deposition on the N-CNF and Co/CoO_x NP surfaces. Analysis of the Pd 3d spectra showed a strong increase in the intensity of the Pd 3d5/2 peak of N-C-Co20-Pd100 that included metal Pd (0) at 335.2 eV and oxide Pd (+II) at 336.3eV (Table S3, Supplementary Materials).

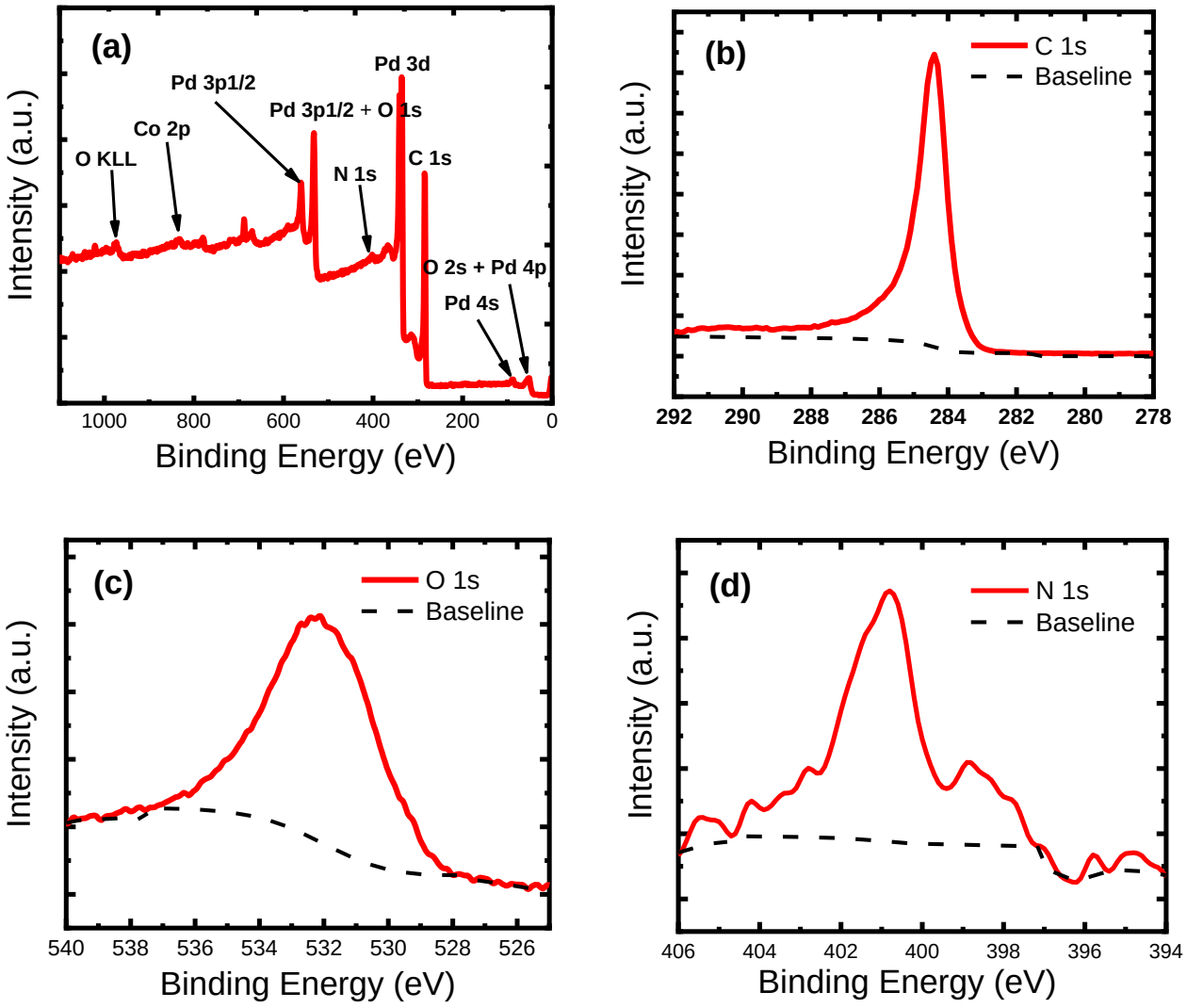

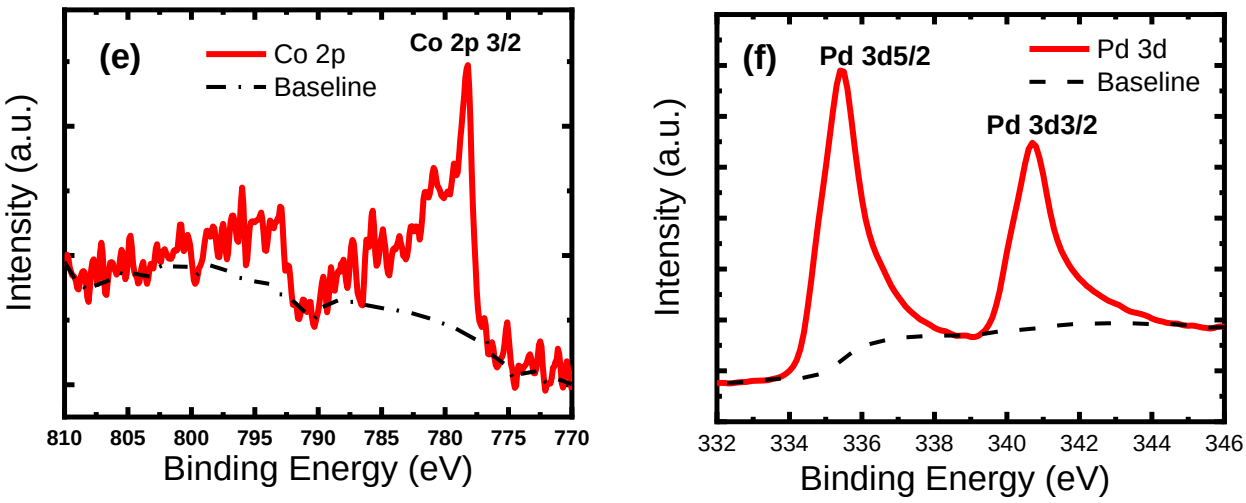

Figure 4. XPS analysis of N-C-Co-Pd electrode samples: (a) representative XPS survey scan; (b) C 1s; (c) O 1s; (d) N 1s; (e) Co 2P; and (f) Pd 3d spectra.

Measurement of the N_2 adsorption/desorption isotherms, surface areas (BET method), and pore size of the different electrodes (Table S4, Supplementary Materials) showed that Co/CoO_x NP *in situ* synthesis inside the N-CNF significantly increased the surface area by 35-fold. This effect might be explained by the formation of degradation products during the thermal steps after electrospinning that promote pore formation. The N-C-Co20 specific surface area was considerably higher than that of N-CNF and N-C-Co10 (239.7 cm^2/g *versus* 6.7 cm^2/g, and 114.1 cm^2/g, with pore diameters of 5.6 nm *versus* 13.8 nm, and 3.8 nm, respectively) (Table S4, Supplementary Materials). A higher specific surface area might enhance electrolyte diffusion into the electrode, and consequently also the electrochemical activity. However, the ALD of Pd NPs on the N-CNF-Co/CoO_x surface slightly reduced the electrode surface area to 150.4 cm^2/g for N-C-Co20-Pd100 (pore diameter of 8.1 nm) and to 113.2 cm^2/g for N-C-Co20-Pd100 (pore diameter of 4.4 nm). The surface area and pore diameter reduction confirmed that ALD efficiently decorated the N-C-Co/CoOx surface and tiny pores between the fibers. The effect of using 100 or 200 ALD cycles on the surface area and the electrode activity during HER/OER will be investigated in the next section.

3.2. Hydrogen Evolution Reactions

The HER polarization LSV curves of the prepared electrodes were illustrated in Figure 5a. HER performance of N-C-Co20-Pd100 has displayed the best electrochemical activity, with a very low overpotential (100 mV) at a current density of 10 mA cm^{-2}, compared with other prepared electrodes of N-CNF (498 mV), N-C-Pd (296 mV), N-C-Co10-Pd200 (167 mV), N-C-Co20-Pd200 (155 mV), and N-C-Co10-Pd100 (148 mV).

Tafel plots were employed in Figure 5b to reveal the HER performance from the kinetic viewpoint. Tafel slopes (determined with the following equation: $\eta=b \log j+a$, where j represents the current density, η the overpotential, and b the Tafel slope)[51] were used to thoroughly investigate the electrocatalytic activity and HER kinetics of the prepared electrodes as listed in (Table S5, Supplementary Materials).

Tafel slope of N-C-Co20-Pd100 is as low as 33 mV dec^{-1}; compared with 73 mV dec^{-1} for N-C-Pd100, , 63 mV dec^{-1} for N-C-Co10-Pd200, 55 mV dec^{-1} for N-C-Co20-Pd200) and 39 mV dec^{-1} for N-C-Co10-Pd100 similar to the reference catalyst (Pt: 36 mV dec^{-1}).[77] As demonstrated in previous studies, a lower Tafel slope is more HER catalysis advantageous since current density can undergo a sharper raise with a low η, thus benefiting HER process (ref). The low b of N-C-Co20-Pd100 may arise from a facile reaction mechanism following Volmer- Tafel reactions, which can be attributed to the lower energy barrier from the thermodynamic respect. Whereby, the multi-step HER reaction comprises an electrochemical Volmer reaction ($H_3O^+ + e^- \rightarrow H_{ads} + H_2O$, 120 mV dec^{-1}), followed by a chemical Tafel reaction ($H_3O^+ + e^- \rightarrow H_{ads} + H_2O$, 120 mV dec^{-1}) or an electrochemical Heyrovsky reaction ($H_{ads} + H_3O^+ + e^- \rightarrow \mathbf{H_2}\uparrow + H_2O$, 40 mV dec^{-1}).

The exchange current density (J_0) was extrapolated from the Tafel plots (Figure 5b) to investigate the intrinsic HER activity of N-C-Co20-Pd100. The highest J_0 value was obtained with N-C-Co20-Pd100 (~1.8 mA cm^{-2}, *versus* 1.13 mA cm^{-2} for C-Pd, 1.5 mA cm^{-2} for N-C-Co10-Pd100, and 1.43 mA cm^{-2} for N-C-Co20-Pd200) (Table S5, Supplementary Materials). Which may result in

the high active site density and the excellent electron transport capacity of N-C-Co10-Pd100. To confirm this, the charge transfers resistance (R_{ct}) values were extrapolated from EIS measurements (Table S5 and Figure 5c in Nyquist plots). The N-C-Co20-Pd100 electrode displayed a smaller R_{ct} value (1.2 Ohm) compared with N-C-Pd100 (7.2 Ohm), N-C-Co10-Pd100 (2.5 Ohm), N-C-Co10-Pd200 (4 Ohm), and N-C-Co20-Pd200 (2.4 Ohm), in agreement with its HER activity results and lower overpotential, due to the higher conductivity and electrical exchange of N-CNF, Co/CoO_x, and Pd NPs. These results indicate that: (i) HER proceeds via a Volmer-Heyrovsky mechanism when using N-CNF electrodes; (ii) increasing the Co/CoO_x content from N-C-Co10 to N-C-Co20 enhances the electrode activity for HER; (iii) increasing the amount of Pd NPs deposited on the electrode surface (from 100 to 200 ALD cycles) negatively affected the electrode activity.[78]

Recent findings indicated that three major parameters are identified control the hydrogen generation activity (HER) in an aqueous system the availability of active sites for the reaction so-called electrochemical active surface area (ECSA).[79] The large surface area and network structure of free-standing electrodes increase effectively the contact area of active surfaces to the electrolyte. In this work, estimation of the ECSA was performed by computing the electrochemical double-layer capacitance (C_{dl}) from CSV plots. The results showed larger ECSA values for N-C-Co20-Pd100 (1750 cm^2) than for N-C-Pd100 (375 cm^2), N-C-Co10-Pd100 (750 cm^2), N-C-Co10-Pd200 (775 cm^2), and N-C-Co20-Pd200 (600 cm^2) (Figure 5d and Table S5). The higher capacitance and ECSA values of the N-C-Co20-Pd100 electrode indicate that it improved HER performance could be explained by its specific porous structure and larger active site surface.

In order to study the electrochemical activity for hydrogen production in presence of the elaborated N-CNF-Co/CoOx nanofiber electrodes. The hydrogen generation using N-C-Co20-Pd100 as a working electrode was monitored for 2 hours (Figure 5e). Measurements of the hydrogen evolution rate and Faraday efficiency have been used to describe the efficiency with which charge (electrons) is transferred between the electrolyte and the electrodes facilitating an HER reaction[80,81].

The current-time curves obtained from chronoamperometry tests for FE measurements of N-C-Co20-Pd100 electrode were illustrated in Fig(S1). The best electrode (N-C-Co20-Pd100) exhibited a high hydrogen evolution rate (250 μmol/h) and excellent faradaic efficiency (~95%) over 2 hr. This high electrochemical performance can be explained by the higher current density (as indicated by LSV measurements) and low R_{ct} value, respectively. The overpotential value was not changed during the 40h chronoamperometry test at 100 mV (Figure 6d). Furthermore, the XRD analysis after the test (Figure 5f) highlighted a slight decrease in the (002) peak intensity for graphitic structure as well as the peaks ascribed to the (111) and (200) planes of the Co/CoO_x NPs. However, no major intensity changes for the typical peaks of Co/CoO_x crystals. This demonstrated the superior durability and chemical stability of the prepared free-standing N-CNF-Co/CoO_x-Pd electrodes.

Literature survey has shown that the N-C-Co20-Pd100 overpotential value was also lower than that of previously reported CNF-based electrodes (Table 5,6) and similar to that of the commercial Pt (100 mV @10 mA cm^{-2}) and Pt/C catalysts (36 mV dec^{-1})[77]. The effect of Pd particle size on the catalyst activity during HER has not been much studied. As Pd NPs with a diameter >10 nm behave like bulk Pd, size affects only below this diameter, particularly in the range of 2-5 nm.[82,83] This can be explained by a geometric effect, and by the induction of structural changes through an epitaxial strain of Pd NPs. Moreover, as Pd NPs display facets with different crystallographic orientations, the catalytic activity might be influenced by size-mediated differences in their relative abundance.[84] Here, the decreased density and size of Pd NPs (from 200 ALD cycles/10 nm to 100 ALD cycles 5 nm) could explain N-C-Co20-Pd100 better electrochemical performance during HER because the electrode electrochemical activity is reduced by Pd NP high surface coverage. Moreover, Pd NP aggregation or Ostwald-ripening during the HER test should be less frequent during 100 ADL cycles due to the lower Pd NP density (i.e. higher distance between Pd NPs).[82]

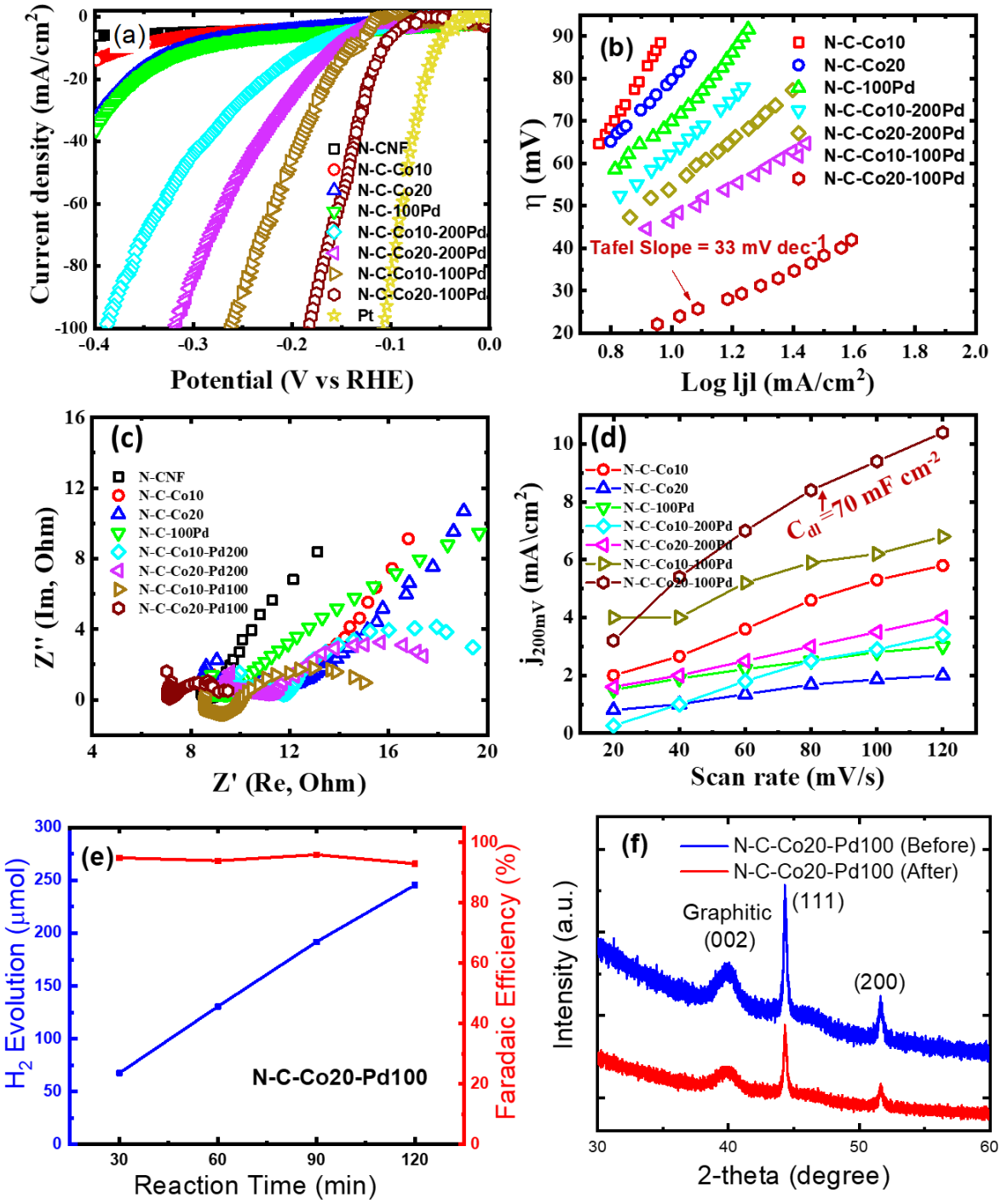

Figure 5. Comparison of the performance of the commercial Pt electrode and the free-standing N-C-Co/CoO_x-Pd electrodes during HER in the presence of 1 M KOH, as electrolyte: (a) Linear sweep voltammetry at 5 mV s^{-1}; (b) Tafel plots of the prepared electrodes; (c) EIS measurements (at a -0.3 V potential vs RHE); (d) electrochemical double-layer capacitance (C_{dl}) represented as linear fit of

the capacitive currents of the catalysts vs. potential scanning rates from 20 mV s1 to 120 mV s1, (e) hydrogen evolution rate and Faradic Efficiency of the electrodes; (f) XRD patterns of the best electrode (N-C-Co20-Pd100) after the chronoamperometric response (j-t) test.

3.3. Oxygen Evolution Reaction

OER is an important process for energy conversion and storage, particularly during water electrolysis. As O∗, HO∗, and HOO∗ are the main OER intermediates, the M-O bonding interaction during OER plays a major role in their stabilization at the surface, and can significantly influence the overall water splitting efficiency.[85] Like for HER, a volcano-type relationship can be observed for OER using (ΔG_{O*} - ΔG_{HO*}) as a descriptor. Many studies focused on Co_3O_4 nanostructures as OER catalysts due to their good activity and stability[86], abundance, low cost, and environmental friendliness. The many active sites present on Co_3O_4 (111) explain the higher electrocatalytic activity of ultrathin Co_3O_4 nanosheets during water and ethanol oxidation in alkaline solutions.[86]

The N-C-Co20-Pd100 electrode exhibited outstanding OER activity with an overpotential of approximately 160 mV at 10 mA cm^{-2} compared with N-CNF (537 mV), N-C-Pd (380 mV), N-C-Co10-Pd100 (270 mV), N-C-Co10-Pd200 (366 mV), and N-C-Co20-Pd200 (290 mV) (Figure 6a). As observed for HER, increasing the amount of Pd NPs deposited on the electrode surface (from 100 to 200 ALD cycles) negatively affected the electrode electrochemical activity. N-C-Co20-Pd100 performance was similar to that of the commercial IrO_2 electrode (210 mV @10 mA cm^{-2}). Moreover, N-C-Co20-Pd100 displayed the smallest Tafel slope value (113 mV dec^{-1} compared with 412 mV dec^{-1} for N-C-Pd100, 158 mV dec^{-1} for N-C-Co10-Pd100, 399 mV dec^{-1} for N-C-Co10-Pd200, and 316 mV dec^{-1} for N-C-Co20-Pd200) that was similar to that of IrO_2 (156 mV dec^{-1}) (Figure 6b).

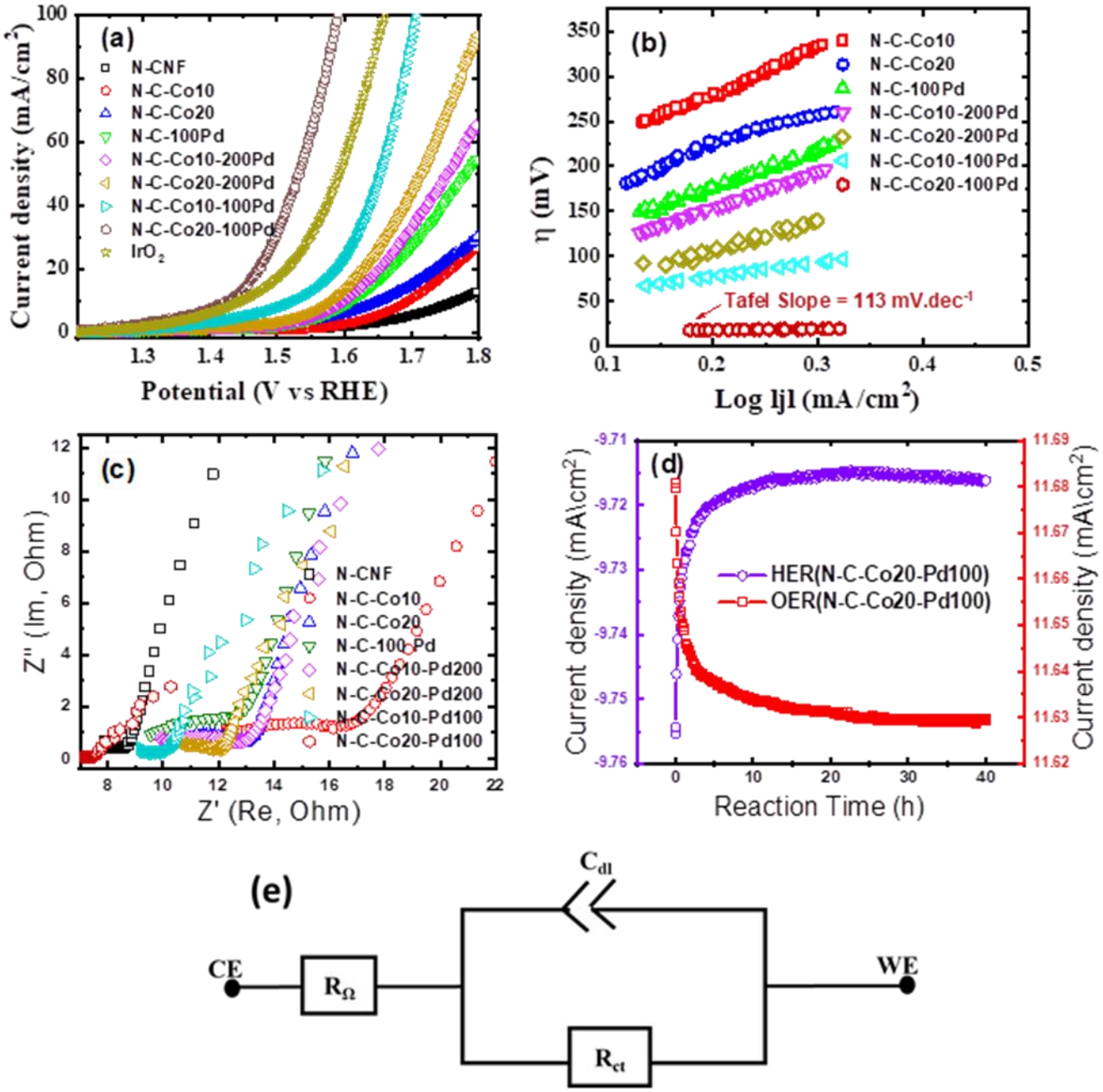

Figure 6. Comparison of the electrocatalytic activity during OER carried out with the commercial IrO_2 electrode and the free-standing N-C-Co-Pd electrodes in the presence of 1 M KOH as the electrolyte. (a) LSV of the different samples. (b) Tafel plots of the prepared electrodes; (c) EIS measurements at 1.6 V vs RHE. Nyquist plots without Warburg impedance; (d) Current density in the function of the reaction time for HER and OER. (e) equivalent circuit applied for evaluation of both (HER and OER) EIS measurements.

N-C-Co20-Pd100 displayed a J_0 (1.22 mA cm^{-2}) considerably more elevated than N-C-Pd (0.53 mA cm^{-2}), N-C-Co10-Pd100 (0.62 mA cm^{-2}), and N-C-Co20-Pd200 (0.55 mA cm^{-2}) (Table S5, Supplementary Materials). This high J_0 value reflects the electrode's higher surface-active area. Moreover, the smaller *R*ct value (EIS measurements) of N-C-Co20-Pd100 (12.5 Ω, compared with 55 Ω for N-C-Pd100, 24 Ω for N-C-Co10-Pd100, 39 Ω for N-C-Co10-Pd200, and 21 Ω for N-C-Co20-Pd200) was in agreement with its higher ECSA (1750 cm^2) (Figure 6c). The chemical stability test has been performed to finally conclude that the N-C-Co20-Pd100 is a promising electrode for HER reaction. The long-term durability of the best electrode (N-C-Co20-Pd100) was assessed by recording its overpotential at −10 mA/cm^2 without iR compensation (**Figure 6d)**. Altogether, these results indicated that the best electrode (N-C-Co20-Pd100) displays excellent activity during HER and OER (lowest overpotential at 10 mA cm^{-2} and smallest Tafel slope) compared with previously reported electrocatalysts (Table S6, Supplementary Materials).[87,88,77,30,89] However, the Pd NP amount used in our experiments was much smaller than what was previously described. Other similar work, Guo et. al.[90] developed strategic atomic layer deposition and electrospinning techniques of cobalt sulfide/nitride composite as efficient bifunctional electrocatalysts for overall water Splitting. The prepared electrodes exhibited overpotentials of 20 mV for HER and 180 mV for OER at a current density of 10 mA cm^{-2} in basic medium. However, the lowest Tafel slope of 54.4 mV dec^{-1} was observed in 0.5 M H_2SO_4 electrolyte.

The equivalent circuit applied for the evaluation of both (HER and OER) EIS measurements is illustrated in **Figure 6e**. A classic expression of this circuit in a Nyquist plot was an incomplete semicircle with a line, which straightens out with decreasing frequency.[91] Such a model under right selected circuit element values to fit well with gathered measurement data as seen in **Figures 6c and 5c**. The simplified Randles cell consists of a solution resistance, double layer capacitance and a charge transfer or a polarization resistance. The double layer capacitance (C_{dl}) is in parallel with the

charge transfer resistance (R_{CT}) and this parallel combination is in series with the ohmic resistance (R_{Ω}) as shown in the Figure 6e.

The OER and HER activity of the prepared electrodes are in the following order N-CNF < N-C-Co10 < N-C-Co20 < N-C-Pd100 < N-C-Co10-Pd200 < N-C-Co20-Pd200 < N-C-Co10-Pd100 < N-C-Co20-Pd100. Where, N-C-Co20-Pd100 manifested excellent electrocatalytic activity in water splitting due to: (i) the optimal Co/CoO_x NP loading on CNFs; (ii) Co/CoO_x NP formation within and on the CNF surface; (iii) N-CNF and Co/CoO_x NP surface decoration with ~5 Pd NPs that modify the electronic structures of N-C-Co/CoO_x electrodes, increase their conductivity, accelerate charge transfer, and enhances their electrochemical activity[61] and stability, resistance to corrosion and possibly chemical stability; (iv) the limited N-C-Co/CoO_x surface and structural decomposition because the Co/CoO_x NP surface is protected by an inert graphitic carbon layer and Pd NPs; (v) the N-CNF architecture that favor gas and electrolyte diffusion during HER/OER; (vi) heterostructures made of various active materials with different HBE (i.e. N-C-Co/CoO_x-Pd) that lead to a better HER activity compared with N-CNF-Co/CoOx and N-CNF-Pd nanofibers, possibly due to the presence of accessible active sites or to the improved interface electronic configuration.[92,93,94] The N-C-Co/CoO_x-Pd electrode heterostructure allows the efficient catalysis of H^+ reduction and H_{ads} desorption in HER, improving HER kinetics and activity.[95]

Conclusion

In this study, solution electrospinning, thermal treatment, and ALD were combined to fabricate N-doped CNF-Co/CoOx-Pd electrodes with high electrocatalytic activity towards HER/OER. The incorporation of Co/CoOx and Pd NPs in CNFs results in excellent electrocatalytic activity and very good chemical stability in alkaline electrolyte solutions. Our results show that combining CNF graphitic nanostructures with Co/CoOx and Pd NPs offers great potential for improving catalyst performance in HER/OER and their chemical stability at a lower cost than with already commercially available catalysts (Pt and IrO_2). The best electrode contained up to 25% of

Co, CoOx in traces, and few Pd NPs (100 ALD cycles), and displayed excellent electrocatalyst activity in HER and OER tests. This could be explained by the synergistic interaction between N-CNFs, Co/CoOx, and Pd NPs at the nanoscale interfaces. Moreover, the N-CNF architecture might underlie the fast gas desorption kinetics. The superior HER activity is explained by the N-CNF electrode architecture with more Co/CoO_x edge sites and fewer Pd NPs that can improve electrocatalytic activity and accelerate electron transfer between graphitic layers, Co/CoO_x, and Pd NPs, ultimately increasing the electrode conductivity and consequently its efficacy during HER. This approach could be adapted for incorporating in CNFs other transition metals and metal alloys (as alternatives to Pt and IrO_2) for HER and OER industrial applications using water. The described N-CNF-Co/CoO_x-Pd NPs can be used as a benchmark for developing HER/OER electrodes for electrolysis, metal-air batteries, and wastewater treatment. ALD of a few Pd NPs with very small diameters could also be exploited for water electrolysis and wastewater electrochemical oxidation.

Conflict of interest

All authors have declared the absence of conflicts of interest relative to their contribution to the present publication.

Acknowledgment

Special thanks to the Egypt-France Joint Driver (Imhotep, Project No. 43990SF, 2020-2022) for financially supporting Dr. Ahmed Barhoum (Project PI from the Egyptian Side) during his research stay at the Institut Européen des Membranes (IEM). Dr. Ahmed Barhoum (Group Leader of NanoStruc, Research Group, Helwan University) would also like to thank the Irish Research Council (hereinafter referred to as 'the Council') for financing his research stay at the School of Chemical Sciences, Dublin City University under grant number (Project ID: GOIPD/2020/340). Authors thank Martine Mallet from the SMI LCPME facility (Université de Lorraine-CNRS–

http://www.lcpme.cnr-nancy.fr) for XPS analysis. TEM analysis was performed by I.I and E.C. were partially supported by H2020-MSCA-RISE-2017, 'Novel 1D photonic metal oxide nanostructures for early-stage cancer detection' (Project number: 778157), and by the Poland National Science Centre (NCN) through the OPUS grant 2019/35/B/ST5/00248.

References

(1) Peter, L. M. Photoelectrochemical Water Splitting. A Status Assessment. *Electroanalysis* **2015**, *27* (4), 864–871. https://doi.org/10.1002/elan.201400587.

(2) El-Maghrabi, H. H.; Barhoum, A.; Nada, A. A.; Moustafa, Y. M.; Seliman, S. M.; Youssef, A. M.; Bechelany, M. Synthesis of Mesoporous Core-Shell CdS@TiO2 (0D and 1D) Photocatalysts for Solar-Driven Hydrogen Fuel Production. *J. Photochem. Photobiol. A Chem.* **2018**, *351*, 261–270. https://doi.org/10.1016/j.jphotochem.2017.10.048.

(3) Nada, A. A.; El Rouby, W. M. A.; Bekheet, M. F.; Antuch, M.; Weber, M.; Miele, P.; Viter, R.; Roualdes, S.; Millet, P.; Bechelany, M. Highly Textured Boron/Nitrogen Co-Doped TiO2 with Honeycomb Structure Showing Enhanced Visible-Light Photoelectrocatalytic Activity. *Appl. Surf. Sci.* **2019**, 144419. https://doi.org/10.1016/J.APSUSC.2019.144419.

(4) Pavlenko, M.; Siuzdak, K.; Coy, E.; Jancelewicz, M.; Jurga, S.; Iatsunskyi, I. Silicon/TiO2 Core-Shell Nanopillar Photoanodes for Enhanced Photoelectrochemical Water Oxidation. *Int. J. Hydrogen Energy* **2017**, *42* (51), 30076–30085. https://doi.org/10.1016/j.ijhydene.2017.10.033.

(5) Roger, I.; Shipman, M. A.; Symes, M. D. Earth-Abundant Catalysts for Electrochemical and Photoelectrochemical Water Splitting. *Nat. Rev. Chem.* **2017**, *1* (1), 0003. https://doi.org/10.1038/s41570-016-0003.

(6) Shalan, A. E.; Barhoum, A.; Elseman, A. M.; Rashad, M. M.; Lira-Cantú, M. Nanofibers as Promising Materials for New Generations of Solar Cells. In *Handbook of Nanofibers*;

Springer International Publishing: Cham, 2018; pp 1–33. https://doi.org/10.1007/978-3-319-42789-8_51-1.

(7) Zhang, S. L.; Guan, B. Y.; Lu, X. F.; Xi, S.; Du, Y.; Lou, X. W. (David). Metal Atom-Doped Co_3O_4 Hierarchical Nanoplates for Electrocatalytic Oxygen Evolution. *Adv. Mater.* **2020**, *32* (31), 2002235. https://doi.org/10.1002/adma.202002235.

(8) El-Maghrabi, H. H.; Nada, A. A.; Roualdes, S.; Bekheet, M. F. Design of Ni/NiO–TiO2/RGO Nanocomposites on Carbon Cloth Conductors via PECVD for Electrocatalytic Water Splitting. *Int. J. Hydrogen Energy* **2020**, *45* (56), 32000–32011.

(9) Du, L.; Qian, K.; Zhu, X.; Yan, X.; Kobayashi, H.; Liu, Z.; Lou, Y.; Li, R. Interface Engineering of Palladium and Zinc Oxide Nanorods with Strong Metal-Support Interactions for Enhanced Hydrogen Production from Base-Free Formaldehyde Solution. *J. Mater. Chem. A* **2019**, *7* (15), 8855–8864. https://doi.org/10.1039/c8ta12019f.

(10) Zhou, T.; Xu, W.; Zhang, N.; Du, Z.; Zhong, C.; Yan, W.; Ju, H.; Chu, W.; Jiang, H.; Wu, C.; Xie, Y. Ultrathin Cobalt Oxide Layers as Electrocatalysts for High-Performance Flexible Zn–Air Batteries. *Adv. Mater.* **2019**, *31* (15), 1807468. https://doi.org/10.1002/adma.201807468.

(11) El-Maghrabi, H. H.; Nada, A. A.; Bekheet, M. F.; Roualdes, S.; Riedel, W.; Iatsunskyi, I.; Coy, E.; Gurlo, A.; Bechelany, M. Coaxial Nanofibers of Nickel/Gadolinium Oxide/Nickel Oxide as Highly Effective Electrocatalysts for Hydrogen Evolution Reaction. *J. Colloid Interface Sci.* **2021**, *587*, 457–466.

(12) Zhao, Y.; Zhang, J.; Li, K.; Ao, Z.; Wang, C.; Liu, H.; Sun, K.; Wang, G. Electrospun Cobalt Embedded Porous Nitrogen Doped Carbon Nanofibers as an Efficient Catalyst for Water Splitting. *J. Mater. Chem. A* **2016**, *4* (33), 12818–12824. https://doi.org/10.1039/C6TA04244A.

(13) Ramanavicius, S.; Ramanavicius, A. Insights in the Application of Stoichiometric and Non-Stoichiometric Titanium Oxides for the Design of Sensors for the Determination of Gases and

Vocs (Tio2−x and Tino2n−1 vs. Tio2). *Sensors (Switzerland)*. MDPI AG December 1, 2020, pp 1–18. https://doi.org/10.3390/s20236833.

(14) Wang, J.; Zhu, H.; Yu, D.; Chen, J.; Chen, J.; Zhang, M.; Wang, L.; Du, M. Engineering the Composition and Structure of Bimetallic Au–Cu Alloy Nanoparticles in Carbon Nanofibers: Self-Supported Electrode Materials for Electrocatalytic Water Splitting. *ACS Appl. Mater. Interfaces* **2017**, *9* (23), 19756–19765. https://doi.org/10.1021/acsami.7b01418.

(15) Wang, J.; Zhu, H.; Chen, J.; Zhang, B.; Zhang, M.; Wang, L.; Du, M. Small and Well-Dispersed Cu Nanoparticles on Carbon Nanofibers: Self-Supported Electrode Materials for Efficient Hydrogen Evolution Reaction. *Int. J. Hydrogen Energy* **2016**, *41* (40), 18044–18049. https://doi.org/10.1016/J.IJHYDENE.2016.08.058.

(16) Li, M.; Zhu, Y.; Wang, H.; Wang, C.; Pinna, N.; Lu, X. Ni Strongly Coupled with Mo $_2$ C Encapsulated in Nitrogen-Doped Carbon Nanofibers as Robust Bifunctional Catalyst for Overall Water Splitting. *Adv. Energy Mater.* **2019**, *9* (10), 1803185. https://doi.org/10.1002/aenm.201803185.

(17) Nnaji, C. O.; Jeevanandam, J.; Chan, Y. S.; Danquah, M. K.; Pan, S.; Barhoum, A. Engineered Nanomaterials for Wastewater Treatment: Current and Future Trends. In *Fundamentals of Nanoparticles*; Elsevier, 2018; pp 129–168. https://doi.org/10.1016/b978-0-323-51255-8.00006-9.

(18) El-maghrabi, H. H.; Ahmed, E.; Soliman, F. S.; Mohamed, Y.; Amin, A. E. One Pot Environmental Friendly Nanocomposite Synthesis of Novel TiO_2 -Nanotubes on Graphene Sheets as Effective Photocatalyst. *Egypt. J. Pet.* **2016**, *25* (4), 575–584. https://doi.org/10.1016/j.ejpe.2015.12.004.

(19) Chen, X.; Cheng, L.; Li, H.; Barhoum, A.; Zhang, Y.; He, X.; Yang, W.; Bubakir, M. M.; Chen, H. Magnetic Nanofibers: Unique Properties, Fabrication Techniques, and Emerging Applications. *ChemistrySelect* **2018**, *3* (31), 9127–9143.

https://doi.org/10.1002/slct.201702480.

(20) Abdel-Haleem, F. M.; Saad, M.; Barhoum, A.; Bechelany, M.; Rizk, M. S. PVC Membrane, Coated-Wire, and Carbon-Paste Ion-Selective Electrodes for Potentiometric Determination of Galantamine Hydrobromide in Physiological Fluids. *Mater. Sci. Eng. C* **2018**, *89*, 140–148. https://doi.org/10.1016/J.MSEC.2018.04.001.

(21) Abdel-Haleem, F. M.; Gamal, E.; Rizk, M. S.; El Nashar, R. M.; Anis, B.; Elnabawy, H. M.; Khalil, A. S. G.; Barhoum, A. T-Butyl Calixarene/Fe2O3@MWCNTs Composite-Based Potentiometric Sensor for Determination of Ivabradine Hydrochloride in Pharmaceutical Formulations. *Mater. Sci. Eng. C* **2020**, *116*, 111110. https://doi.org/10.1016/j.msec.2020.111110.

(22) Abdel-Haleem, F. M.; Gamal, E.; Rizk, M. S.; El Nashar, R. M.; Anis, B.; Elnabawy, H. M.; Khalil, A. S. G.; Barhoum, A. T-Butyl Calixarene/Fe2O3@MWCNTs Composite-Based Potentiometric Sensor for Determination of Ivabradine Hydrochloride in Pharmaceutical Formulations. *Mater. Sci. Eng. C* **2020**, *116*, 111110. https://doi.org/10.1016/j.msec.2020.111110.

(23) Abdel-Haleem, F. M.; Mahmoud, S.; Abdel-Ghani, N. E. T.; El Nashar, R. M.; Bechelany, M.; Barhoum, A. Polyvinyl Chloride Modified Carbon Paste Electrodes for Sensitive Determination of Levofloxacin Drug in Serum, Urine, and Pharmaceutical Formulations. *Sensors* **2021**, *21* (9), 3150. https://doi.org/10.3390/s21093150.

(24) Abdel-Haleem, F. M.; Gamal, E.; Rizk, M. S.; Madbouly, A.; El Nashar, R. M.; Anis, B.; Elnabawy, H. M.; Khalil, A. S. G.; Barhoum, A. Molecularly Imprinted Electrochemical Sensor-Based Fe2O3@MWCNTs for Ivabradine Drug Determination in Pharmaceutical Formulation, Serum, and Urine Samples. *Front. Bioeng. Biotechnol.* **2021**, *9* (April), 1–16. https://doi.org/10.3389/fbioe.2021.648704.

(25) Abdel-Haleem, F. M.; Gamal, E.; Rizk, M. S.; Madbouly, A.; El Nashar, R. M.; Anis, B.;

Elnabawy, H. M.; Khalil, A. S. G.; Barhoum, A. Molecularly Imprinted Electrochemical Sensor-Based Fe2O3@MWCNTs for Ivabradine Drug Determination in Pharmaceutical Formulation, Serum, and Urine Samples. *Front. Bioeng. Biotechnol.* **2021**, *9*, 213. https://doi.org/10.3389/fbioe.2021.648704.

(26) Haichao, L.; Haoyi, L.; Bubakir, M. M.; Weimin, Y.; Barhoum, A. Engineering Nanofibers as Electrode and Membrane Materials for Batteries, Supercapacitors, and Fuel Cells. In *Handbook of Nanofibers*; Springer International Publishing: Cham, 2018; pp 1–27. https://doi.org/10.1007/978-3-319-42789-8_52-1.

(27) Barhoum, A.; Samyn, P.; Öhlund, T.; Dufresne, A. Review of Recent Research on Flexible Multifunctional Nanopapers. *Nanoscale* **2017**, *9* (40), 15181–15205. https://doi.org/10.1039/c7nr04656a.

(28) Sawy, A. M.; Barhoum, A.; Abdel Gaber, S. A.; El-Hallouty, S. M.; Shousha, W. G.; Maarouf, A. A.; Khalil, A. S. G. Insights of Doxorubicin Loaded Graphene Quantum Dots: Synthesis, DFT Drug Interactions, and Cytotoxicity. *Mater. Sci. Eng. C* **2021**, *122*, 111921. https://doi.org/10.1016/j.msec.2021.111921.

(29) Rasouli, R.; Barhoum, A.; Bechelany, M.; Dufresne, A. Nanofibers for Biomedical and Healthcare Applications. *Macromol. Biosci.* **2019**, *19* (2). https://doi.org/10.1002/mabi.201800256.

(30) Ding, Q.; Liu, M.; Miao, Y.-E.; Huang, Y.; Liu, T. Electrospun Nickel-Decorated Carbon Nanofiber Membranes as Efficient Electrocatalysts for Hydrogen Evolution Reaction. *Electrochim. Acta* **2015**, *159*, 1–7. https://doi.org/10.1016/J.ELECTACTA.2015.01.197.

(31) Wang, Y.; Zhang, G.; Xu, W.; Wan, P.; Lu, Z.; Li, Y.; Sun, X. A 3D Nanoporous Ni-Mo Electrocatalyst with Negligible Overpotential for Alkaline Hydrogen Evolution. *ChemElectroChem* **2014**, *1* (7), 1138–1144. https://doi.org/10.1002/celc.201402089.

(32) Kawashima, A.; Akiyama, E.; Habazaki, H.; Hashimoto, K. Characterization of Sputter-

Deposited Ni-Mo and Ni-W Alloy Electrocatalysts for Hydrogen Evolution in Alkaline Solution. *Mater. Sci. Eng. A* **1997**, *226–228*, 905–909. https://doi.org/10.1016/S0921-5093(97)80095-0.

(33) Li, S.; Wang, Y.; Peng, S.; Zhang, L.; Al-Enizi, A. M.; Zhang, H.; Sun, X.; Zheng, G. Co-Ni-Based Nanotubes/Nanosheets as Efficient Water Splitting Electrocatalysts. *Adv. Energy Mater.* **2016**, *6* (3), 1501661. https://doi.org/10.1002/aenm.201501661.

(34) Han, L.; Dong, S.; Wang, E. Transition-Metal (Co, Ni, and Fe)-Based Electrocatalysts for the Water Oxidation Reaction. *Adv. Mater.* **2016**, *28* (42), 9266–9291. https://doi.org/10.1002/adma.201602270.

(35) Navarro-Flores, E.; Chong, Z.; Omanovic, S. Characterization of Ni, NiMo, NiW and NiFe Electroactive Coatings as Electrocatalysts for Hydrogen Evolution in an Acidic Medium. *J. Mol. Catal. A Chem.* **2005**, *226* (2), 179–197. https://doi.org/10.1016/J.MOLCATA.2004.10.029.

(36) Coy, E.; Yate, L.; Valencia, D. P.; Aperador, W.; Siuzdak, K.; Torruella, P.; Azanza, E.; Estrade, S.; Iatsunskyi, I.; Peiro, F.; Zhang, X.; Tejada, J.; Ziolo, R. F. High Electrocatalytic Response of a Mechanically Enhanced NbC Nanocomposite Electrode Toward Hydrogen Evolution Reaction. *ACS Appl. Mater. Interfaces* **2017**, *9* (36), 30872–30879. https://doi.org/10.1021/acsami.7b10317.

(37) Valencia, D. P.; Yate, L.; Aperador, W.; Li, Y.; Coy, E. High Electrocatalytic Response of Ultra-Refractory Ternary Alloys of Ta-Hf-C Carbide toward Hydrogen Evolution Reaction in Acidic Media. *J. Phys. Chem. C* **2018**, *122* (44), 25433–25440. https://doi.org/10.1021/acs.jpcc.8b08123.

(38) Lu, X. F.; Yu, L.; Zhang, J.; Lou, X. W. (David). Ultrafine Dual-Phased Carbide Nanocrystals Confined in Porous Nitrogen-Doped Carbon Dodecahedrons for Efficient Hydrogen Evolution Reaction. *Adv. Mater.* **2019**, *31* (30), 1900699. https://doi.org/10.1002/adma.201900699.

(39) Weber, M. J.; Verheijen, M. A.; Bol, A. A.; Kessels, W. M. M. Sub-Nanometer Dimensions Control of Core/Shell Nanoparticles Prepared by Atomic Layer Deposition. *Nanotechnology* **2015**, *26* (9). https://doi.org/10.1088/0957-4484/26/9/094002.

(40) Topuz, F.; Uyar, T. Atomic Layer Deposition of Palladium Nanoparticles on a Functional Electrospun Poly-Cyclodextrin Nanoweb as a Flexible and Reusable Heterogeneous Nanocatalyst for the Reduction of Nitroaromatic Compounds. *Nanoscale Adv.* **2019**, *1* (10), 4082–4089. https://doi.org/10.1039/c9na00368a.

(41) Celebioglu, A.; Ranjith, K. S.; Eren, H.; Biyikli, N.; Uyar, T. Surface Decoration of Pt Nanoparticles via ALD with TiO2 Protective Layer on Polymeric Nanofibers as Flexible and Reusable Heterogeneous Nanocatalysts. *Sci. Rep.* **2017**, *7* (1), 13401. https://doi.org/10.1038/s41598-017-13805-2.

(42) Lu, J.; Low, K.-B.; Lei, Y.; Libera, J. A.; Nicholls, A.; Stair, P. C.; Elam, J. W. Toward Atomically-Precise Synthesis of Supported Bimetallic Nanoparticles Using Atomic Layer Deposition. *Nat. Commun.* **2014**, *5* (1), 3264. https://doi.org/10.1038/ncomms4264.

(43) Cao, K.; Zhu, Q.; Shan, B.; Chen, R. Controlled Synthesis of Pd/Pt Core Shell Nanoparticles Using Area-Selective Atomic Layer Deposition. *Sci. Rep.* **2015**, *5* (1), 8470. https://doi.org/10.1038/srep08470.

(44) Kertmen, A.; Barbé, E.; Szkoda, M.; Siuzdak, K.; Babačić, V.; Torruella, P.; Iatsunskyi, I.; Kotkowiak, M.; Rytel, K.; Estradé, S.; Peiró, F.; Jurga, S.; Li, Y.; Coy, E. Photoelectrochemically Active N-Adsorbing Ultrathin TiO 2 Layers for Water-Splitting Applications Prepared by Pyrolysis of Oleic Acid on Iron Oxide Nanoparticle Surfaces under Nitrogen Environment. *Adv. Mater. Interfaces* **2019**, *6* (3). https://doi.org/10.1002/admi.201801286.

(45) Cheng, N.; Liu, J.; Sun, X. Electrocatalysts by Atomic Layer Deposition for Fuel Cell Applications. *Nano Energy* **2016**, *29*, 220–242.

https://doi.org/10.1016/J.NANOEN.2016.01.016.

(46) Liu, L. Atomic Layer Deposition of Electrocatalysts for Use in Fuel Cells and Electrolyzers. In *Atomic Layer Deposition in Energy Conversion Applications*; Wiley-VCH Verlag GmbH & Co. KGaA: Weinheim, Germany, 2017; pp 149–181. https://doi.org/10.1002/9783527694822.ch5.

(47) George, S. M. Atomic Layer Deposition: An Overview. *Chem. Rev.* **2010**, *110* (1), 111–131. https://doi.org/10.1021/cr900056b.

(48) Johnson, R. W.; Hultqvist, A.; Bent, S. F. A Brief Review of Atomic Layer Deposition: From Fundamentals to Applications. *Mater. Today* **2014**, *17* (5), 236–246. https://doi.org/10.1016/J.MATTOD.2014.04.026.

(49) Song, Z.; Banis, M. N.; Zhang, L.; Wang, B.; Yang, L.; Banham, D.; Zhao, Y.; Liang, J.; Zheng, M.; Li, R.; Ye, S.; Sun, X. Origin of Achieving the Enhanced Activity and Stability of Pt Electrocatalysts with Strong Metal-Support Interactions via Atomic Layer Deposition. *Nano Energy* **2018**, *53*, 716–725. https://doi.org/10.1016/J.NANOEN.2018.09.008.

(50) Anitha, V. C.; Zazpe, R.; Krbal, M.; Yoo, J.; Sopha, H.; Prikryl, J.; Cha, G.; Slang, S.; Schmuki, P.; Macak, J. M. Anodic TiO2 Nanotubes Decorated by Pt Nanoparticles Using ALD: An Efficient Electrocatalyst for Methanol Oxidation. *J. Catal.* **2018**, *365*, 86–93. https://doi.org/10.1016/J.JCAT.2018.06.017.

(51) Young, K. M. H.; Hamann, T. W. Enhanced Photocatalytic Water Oxidation Efficiency with Ni(OH) 2 Catalysts Deposited on α-Fe 2 O 3 via ALD. *Chem. Commun.* **2014**, *50* (63), 8727. https://doi.org/10.1039/C4CC02598A.

(52) Guterman, V. E.; Belenov, S. V.; Alekseenko, A. A.; Lin, R.; Tabachkova, N. Y.; Safronenko, O. I. Activity and Stability of Pt/C and Pt-Cu/C Electrocatalysts. *Electrocatalysis* **2018**, *9* (5), 550–562. https://doi.org/10.1007/s12678-017-0451-1.

(53) Barhoum, A.; Rasouli, R.; Yousefzadeh, M.; Rahier, H.; Bechelany, M. Nanofiber

Technology: History and Developments. In *Handbook of Nanofibers*; Springer International Publishing: Cham, 2018; pp 1–42. https://doi.org/10.1007/978-3-319-42789-8_54-1.

(54) Merenda, A.; Weber, M.; Bechelany, M.; Allioux, F. M.; Hyde, L.; Kong, L.; Dumée, L. F. Fabrication of Pd-TiO 2 Nanotube Photoactive Junctions via Atomic Layer Deposition for Persistent Pesticide Pollutants Degradation. *Appl. Surf. Sci.* **2019**, *483*, 219–230. https://doi.org/10.1016/j.apsusc.2019.03.285.

(55) Weber, M.; Collot, P.; El Gaddari, H.; Tingry, S.; Bechelany, M.; Holade, Y. Enhanced Catalytic Glycerol Oxidation Activity Enabled by Activated-Carbon-Supported Palladium Catalysts Prepared through Atomic Layer Deposition. *ChemElectroChem* **2018**, *5* (5), 743–747. https://doi.org/10.1002/celc.201701196.

(56) Liu, R.; Gu, S.; Du, H.; Li, C. M. Controlled Synthesis of FeP Nanorod Arrays as Highly Efficient Hydrogen Evolution Cathode. *J. Mater. Chem. A* **2014**, *2* (41), 17263–17267. https://doi.org/10.1039/c4ta03638g.

(57) Barhoum, A.; Pal, K.; Rahier, H.; Uludag, H.; Kim, I. S.; Bechelany, M. Nanofibers as New-Generation Materials: From Spinning and Nano-Spinning Fabrication Techniques to Emerging Applications. *Appl. Mater. Today* **2019**, *17*, 1–35. https://doi.org/10.1016/j.apmt.2019.06.015.

(58) Wanjun, T.; Donghua, C. Mechanism of Thermal Decomposition of Cobalt Acetate Tetrahydrate. *Chem. Pap.* **2007**, *61* (4), 329–332. https://doi.org/10.2478/s11696-007-0042-3.

(59) Luo, Q. X.; Guo, L. P.; Yao, S. Y.; Bao, J.; Liu, Z. T.; Liu, Z. W. Cobalt Nanoparticles Confined in Carbon Matrix for Probing the Size Dependence in Fischer-Tropsch Synthesis. *J. Catal.* **2019**, 143–156. https://doi.org/10.1016/j.jcat.2018.11.002.

(60) Topuz, F.; Celebioglu, A.; Aytac, Z.; Uyar, T. Influence of Salt Addition on Polymer-Free Electrospinning of Cyclodextrin Nanofibers. *Nano Express* **2020**, *1* (2), 020041. https://doi.org/10.1088/2632-959x/abb6c5.

(61) Barhoum, A.; El-Maghrabi, H. H.; Iatsunskyi, I.; Coy, E.; Renard, A.; Salameh, C.; Weber, M.; Sayegh, S.; Nada, A. A.; Roualdes, S.; Bechelany, M. Atomic Layer Deposition of Pd Nanoparticles on Self-Supported Carbon-Ni/NiO-Pd Nanofiber Electrodes for Electrochemical Hydrogen and Oxygen Evolution Reactions. *J. Colloid Interface Sci.* **2020**, *569*, 286–297. https://doi.org/10.1016/j.jcis.2020.02.063.

(62) Liu, Y.; Teng, H.; Hou, H.; You, T. Nonenzymatic Glucose Sensor Based on Renewable Electrospun Ni Nanoparticle-Loaded Carbon Nanofiber Paste Electrode. *Biosens. Bioelectron.* **2009**, *24* (11), 3329–3334. https://doi.org/10.1016/j.bios.2009.04.032.

(63) Maiyalagan, T.; Scott, K. Performance of Carbon Nanofiber Supported Pd-Ni Catalysts for Electro-Oxidation of Ethanol in Alkaline Medium. *J. Power Sources* **2010**, *195* (16), 5246–5251. https://doi.org/10.1016/j.jpowsour.2010.03.022.

(64) Guo, Q.; Liu, D.; Zhang, X.; Li, L.; Hou, H.; Niwa, O.; You, T. Pd–Ni Alloy Nanoparticle/Carbon Nanofiber Composites: Preparation, Structure, and Superior Electrocatalytic Properties for Sugar Analysis. *Anal. Chem.* **2014**, *86* (12), 5898–5905. https://doi.org/10.1021/ac500811j.

(65) Zhu, S.; Sun, J.; Wu, T.; Su, X.; Su, H.; Qu, S.; Xie, Y.; Chen, M.; Diao, G. Graphitized Porous Carbon Nanofibers Prepared by Electrospinning as Anode Materials for Lithium Ion Batteries. *RSC Adv.* **2016**, *6* (86), 83185–83195. https://doi.org/10.1039/C6RA15076D.

(66) Barhoum, A.; García-Betancourt, M. L.; Rahier, H.; Van Assche, G. Physicochemical Characterization of Nanomaterials: Polymorph, Composition, Wettability, and Thermal Stability. In *Emerging Applications of Nanoparticles and Architectural Nanostructures: Current Prospects and Future Trends*; Elsevier Inc., 2018; pp 255–278. https://doi.org/10.1016/B978-0-323-51254-1.00009-9.

(67) Nada, A. A.; Nasr, M.; Viter, R.; Miele, P.; Roualdes, S.; Bechelany, M. Mesoporous ZnFe2O4@TiO2 Nanofibers Prepared by Electrospinning Coupled to PECVD as Highly

Performing Photocatalytic Materials. *J. Phys. Chem. C* **2017**, *121* (39). https://doi.org/10.1021/acs.jpcc.7b08567.

(68) El-Sheikh, S. M.; Barhoum, A.; El-Sherbiny, S.; Morsy, F.; El-Midany, A. A.-H.; Rahier, H. Preparation of Superhydrophobic Nanocalcite Crystals Using Box–Behnken Design. *Arab. J. Chem.* **2019**, *12* (7), 479–1486. https://doi.org/10.1016/j.arabjc.2014.11.003.

(69) Barhoum, A.; Van Assche, G.; Makhlouf, A. S. H.; Terryn, H.; Baert, K.; Delplancke, M.-P.; El-Sheikh, S. M.; Rahier, H. A Green, Simple Chemical Route for the Synthesis of Pure Nanocalcite Crystals. *Cryst. Growth Des.* **2015**, *15* (2). https://doi.org/10.1021/cg501121t.

(70) Ji, L.; Lin, Z.; Alcoutlabi, M.; Toprakci, O.; Yao, Y.; Xu, G.; Li, S.; Zhang, X. Electrospun Carbon Nanofibers Decorated with Various Amounts of Electrochemically-Inert Nickel Nanoparticles for Use as High-Performance Energy Storage Materials. *RSC Adv.* **2012**, *2* (1), 192–198. https://doi.org/10.1039/c1ra00676b.

(71) Yuan, X.; Hu, X.-X.; Ding, X.-L.; Kong, H.-C.; Sha, H.-D.; Lin, H.; Wen, W.; Shen, G.; Guo, Z.; Ma, Z.-F.; Yang, Y. Effects of Cobalt Precursor on Pyrolyzed Carbon-Supported Cobalt-Polypyrrole as Electrocatalyst toward Oxygen Reduction Reaction. *Nanoscale Res. Lett.* **2013**, *8* (1), 478. https://doi.org/10.1186/1556-276X-8-478.

(72) Zhu, J.; Jasper, S.; Zhang, X. Chemical Characterization of Electrospun Nanofibers. In *Electrospun Nanofibers*; Elsevier, 2017; pp 181–206. https://doi.org/10.1016/B978-0-08-100907-9.00008-8.

(73) Bao, G.; Bai, J.; Li, C. Synergistic Effect of the Pd–Ni Bimetal/Carbon Nanofiber Composite Catalyst in Suzuki Coupling Reaction. *Org. Chem. Front.* **2019**, *6* (3), 352–361. https://doi.org/10.1039/C8QO01100A.

(74) Larrude, D. G.; Ayala, P.; Costa, M. E. H. M. da; Freire, F. L. Multiwalled carbon nanotubes decorated with cobalt oxide nanoparticles | Journal of Nanomaterials https://dl.acm.org/doi/10.1155/2012/695453 (accessed Aug 2, 2020).

(75) Guo, S. X.; Liu, Y.; Bond, A. M.; Zhang, J.; Esakki Karthik, P.; Maheshwaran, I.; Senthil Kumar, S.; Phani, K. L. N. Facile Electrochemical Co-Deposition of a Graphene-Cobalt Nanocomposite for Highly Efficient Water Oxidation in Alkaline Media: Direct Detection of Underlying Electron Transfer Reactions under Catalytic Turnover Conditions. *Phys. Chem. Chem. Phys.* **2014**, *16* (35), 19035–19045. https://doi.org/10.1039/c4cp01608d.

(76) Di Blasi, A.; Busacca, C.; Di Blasi, O.; Briguglio, N.; Antonucci, V. Synthesis and Characterization of Electrospun Nickel-Carbon Nanofibers as Electrodes for Vanadium Redox Flow Battery. *J. Electrochem. Soc.* **2018**, *165* (7), A1478–A1485. https://doi.org/10.1149/2.1081807jes.

(77) Chen, J.; Chen, J.; Yu, D.; Zhang, M.; Zhu, H.; Du, M. Carbon Nanofiber-Supported PdNi Alloy Nanoparticles as Highly Efficient Bifunctional Catalysts for Hydrogen and Oxygen Evolution Reactions. *Electrochim. Acta* **2017**, *246*, 17–26. https://doi.org/10.1016/J.ELECTACTA.2017.06.047.

(78) Patil, B.; Satilmis, B.; Khalily, M. A.; Uyar, T. Atomic Layer Deposition of NiOOH/Ni(OH) $_2$ on PIM-1-Based N-Doped Carbon Nanofibers for Electrochemical Water Splitting in Alkaline Medium. *ChemSusChem* **2019**, *12* (7), 1469–1477. https://doi.org/10.1002/cssc.201802500.

(79) Mahmood, N.; Yao, Y.; Zhang, J. W.; Pan, L.; Zhang, X.; Zou, J. J. Electrocatalysts for Hydrogen Evolution in Alkaline Electrolytes: Mechanisms, Challenges, and Prospective Solutions. *Advanced Science*. Wiley-VCH Verlag February 1, 2018. https://doi.org/10.1002/advs.201700464.

(80) Kawrani, S.; Boulos, M.; Bekheet, M. F.; Viter, R.; Nada, A. A.; Riedel, W.; Roualdes, S.; Cornu, D.; Bechelany, M. Segregation of Copper Oxide on Calcium Copper Titanate Surface Induced by Graphene Oxide for Water Splitting Applications. *Appl. Surf. Sci.* **2020**, 146051. https://doi.org/10.1016/j.apsusc.2020.146051.

(81) Kawrani, S.; Nada, A. A.; Bekheet, M. F.; Boulos, M.; Viter, R.; Roualdes, S.; Miele, P.;

Cornu, D.; Bechelany, M. Enhancement of Calcium Copper Titanium Oxide Photoelectrochemical Performance Using Boron Nitride Nanosheets. *Chem. Eng. J.* **2020**, *389*. https://doi.org/10.1016/j.cej.2020.124326.

(82) Khalily, M. A.; Patil, B.; Yilmaz, E.; Uyar, T. Atomic Layer Deposition of Pd Nanoparticles on N-Doped Electrospun Carbon Nanofibers: Optimization of ORR Activity of Pd-Based Nanocatalysts by Tuning Their Nanoparticle Size and Loading. *ChemNanoMat* **2019**, *5* (12), 1540–1546. https://doi.org/10.1002/cnma.201900483.

(83) Gao, G.; Niu, X.; Xu, B.; Wang, X. L.; Yao, Y. F. Shape and Size Effects on Photocatalytic Hydrogen Production: Via Pd/C3N4photocatalysts under Visible Light. *Catal. Sci. Technol.* **2020**, *10* (16), 5438–5442. https://doi.org/10.1039/d0cy00354a.

(84) Navlani-García, M.; Mori , K.; Nozaki, A.; Kuwahara , Y.; Yamashita , H. Investigation of Size Sensitivity in the Hydrogen Production from Formic Acid over Carbon-Supported Pd Nanoparticles. *ChemistrySelect* **2016**, *1* (9), 1879–1886. https://doi.org/10.1002/slct.201600559.

(85) Lee, Y.; Suntivich, J.; May, K. J.; Perry, E. E.; Shao-Horn, Y. Synthesis and Activities of Rutile IrO_2 and RuO_2 Nanoparticles for Oxygen Evolution in Acid and Alkaline Solutions. *J. Phys. Chem. Lett.* **2012**, 399–404. https://doi.org/10.1021/jz2016507.

(86) Cai, Z.; Yao, Q.; Chen, X.; Wang, X. Nanomaterials With Different Dimensions for Electrocatalysis. In *Novel Nanomaterials for Biomedical, Environmental and Energy Applications*; Elsevier, 2018; pp 435–464. https://doi.org/10.1016/B978-0-12-814497-8.00014-X.

(87) Wu, Z.; Lu, X. F.; Zang, S.; Lou, X. W. (David). Non-Noble-Metal-Based Electrocatalysts toward the Oxygen Evolution Reaction. *Adv. Funct. Mater.* **2020**, *30* (15), 1910274. https://doi.org/10.1002/adfm.201910274.

(88) Wu, Z.-Y.; Ji, W.-B.; Hu, B.-C.; Liang, H.-W.; Xu, X.-X.; Yu, Z.-L.; Li, B.-Y.; Yu, S.-H.

Partially Oxidized Ni Nanoparticles Supported on Ni-N Co-Doped Carbon Nanofibers as Bifunctional Electrocatalysts for Overall Water Splitting. *Nano Energy* **2018**, *51*, 286–293. https://doi.org/10.1016/J.NANOEN.2018.06.071.

(89) Li, M.; Zhu, Y.; Song, N.; Wang, C.; Lu, X. Fabrication of Pt Nanoparticles on Nitrogen-Doped Carbon/Ni Nanofibers for Improved Hydrogen Evolution Activity. *J. Colloid Interface Sci.* **2018**, *514*, 199–207. https://doi.org/10.1016/J.JCIS.2017.12.028.

(90) Guo, D.; Wang, J.; Zhang, L.; Chen, X.; Wan, Z.; Xi, B. Strategic Atomic Layer Deposition and Electrospinning of Cobalt Sulfide/Nitride Composite as Efficient Bifunctional Electrocatalysts for Overall Water Splitting. *Small* **2020**, *16* (35), 2002432. https://doi.org/10.1002/smll.202002432.

(91) Ramanavicius, A.; Genys, P.; Ramanaviciene, A. Electrochemical Impedance Spectroscopy Based Evaluation of 1,10-Phenanthroline-5,6-Dione and Glucose Oxidase Modified Graphite Electrode. *Electrochim. Acta* **2014**, *146*, 659–665. https://doi.org/10.1016/j.electacta.2014.08.130.

(92) Sun, J.; Liu, J.; Chen, H.; Han, X.; Wu, Y.; He, J.; Han, C.; Yang, G.; Shan, Y. Strongly Coupled Mo2C and Ni Nanoparticles with In-Situ Formed Interfaces Encapsulated by Porous Carbon Nanofibers for Efficient Hydrogen Evolution Reaction under Alkaline Conditions. *J. Colloid Interface Sci.* **2019**, *558*, 100–105. https://doi.org/10.1016/j.jcis.2019.09.102.

(93) Xu, J.; Liu, T.; Li, J.; Li, B.; Liu, Y.; Zhang, B.; Xiong, D.; Amorim, I.; Li, W.; Liu, L. Boosting the Hydrogen Evolution Performance of Ruthenium Clusters through Synergistic Coupling with Cobalt Phosphide. *Energy Environ. Sci.* **2018**, *11* (7), 1819–1827. https://doi.org/10.1039/c7ee03603e.

(94) Xu, J.; Li, J.; Xiong, D.; Zhang, B.; Liu, Y.; Wu, K. H.; Amorim, I.; Li, W.; Liu, L. Trends in Activity for the Oxygen Evolution Reaction on Transition Metal (M = Fe, Co, Ni) Phosphide Pre-Catalysts. *Chem. Sci.* **2018**, *9* (14), 3470–3476. https://doi.org/10.1039/c7sc05033j.

(95) Lin, H.; Zhang, W.; Shi, Z.; Che, M.; Yu, X.; Tang, Y.; Gao, Q. Electrospinning Hetero-Nanofibers of Fe $_3$ C-Mo $_2$ C/Nitrogen-Doped-Carbon as Efficient Electrocatalysts for Hydrogen Evolution. *ChemSusChem* **2017**, *10* (12), 2597–2604. https://doi.org/10.1002/cssc.201700207.